INTERNATIONAL JOURNAL FOR NUMERICAL METHODS IN FLUIDS, VOL. 10, 481–517 (1990)

SPECTRAL SIMULATIONS OF OSCILLATORY CONVECTION AT LOW PRANDTL NUMBER

J. P. PULICANI

Laboratoire de Mathématiques, Université de Nice, Parc Valrose F-06034 Nice Cedex, France

E. CRESPO DEL ARCO

UNED, Dpto Fisica Fund., Apdo 60141, E-28080, Madrid, Spain

A. RANDRIAMAMPIANINA AND P. BONTOUX

IMFM, 1 rue Honnorat, F-13003 Marseille, France

AND

R. PEYRET

Laboratoire de Mathématiques, Université de Nice, Parc Valrose F-06034 Nice Cedex, France

SUMMARY

Pseudospectral methods are used for the computation of the time-dependent convective flows which arise in shallow cavities filled with low-Prandtl-number liquids when submitted to a horizontal temperature gradient. In similar situations several former numerical results have been shown to disagree about the determination of the threshold of oscillations and about the subsequent supercritical regimes. Two different tau–Chebyshev methods based on the vorticity–streamfunction formulation and using multistep time schemes are considered. Their results are discussed to assess the validity of the solutions. The physical problems concern rectangular cavities which involve either a rigid or a stress-free top wall and either conducting or insulating horizontal walls. Aside from the prediction of the onset of oscillations, which is discussed in the various situations with respect to the results of linear and non-linear analyses and to other computational results, the present study exhibits some bifurcation sequences and a hysteresis cycle at moderate Grashof numbers which are associated to the occurrence of multiple solutions.

KEY WORDS Spectral methods Chebyshev polynomials Navier–Stokes equations Time-dependent convection

INTRODUCTION

The hydrodynamics of crystal growth from melts has been the subject of a number of papers during the last 10 years. A survey of the questions involved can be found, for example, in References 1–3. The difficulties of direct numerical simulation of complex systems involving thermosolutal convection coupled with interface morphology have been evoked, for example, in References 4–6. One of the major causes of striations in grown crystals was established to be the mechanism of stable and periodic temperature fluctuations in the liquid phase. The occurrence of an oscillatory motion superimposed upon a steady convective flow has been observed experimentally by Hurle *et al.*[7] for molten gallium inside a rectangular boat when the imposed horizontal temperature gradient is larger than a critical value (see also References 8–10). The oscillatory behaviour occurring during the transient to the steady state has been extensively analysed by Patterson[11] (see also References 12 and 13). Busse[14] and Clever and Busse[15] have

0271–2091/90/050481–37$18.50

Received 28 September 1988
Revised 7 March 1989

shown in the case of low-Prandtl-number fluid layers heated from below that the oscillatory instability of two-dimensional rolls is caused mainly by the action of momentum advection terms. The stability with respect to two- and three-dimensional disturbances has been analysed by Hart,[16,17] Gill[18] and, recently, by Laure and Roux[19] in the case of a single-cell flow thermally driven by an imposed horizontal temperature gradient (known as the Hadley circulation) inside a shallow layer for a variety of dynamical and thermal conditions. For the rigid–free case (R–F) the critical mode corresponds to a longitudinal two-dimensional oscillatory mode with reduced (with respect to height) wavelength $\lambda_x = 4{\cdot}6$ for Prandtl number $Pr < 0{\cdot}0045$ when the horizontal walls are insulating and $Pr < 0{\cdot}077$ when the horizontal walls are conducting. The transition occurs towards three-dimensional oscillatory modes for larger values of Pr. For the rigid–rigid case (R–R) the critical flow involves transverse two-dimensional steady modes for $Pr < 0{\cdot}034$ with insulating conditions and for $Pr < 0{\cdot}114$ with conducting conditions with the same reduced wavelength $\lambda_x = 2{\cdot}34$. However, these studies do not involve any lateral confinement effect so that they are valid only to give guides for the fundamental trends of the solution according to the values of the physical parameters, namely the Grashof number Gr and the Prandtl number Pr.

The lateral walls have a stabilizing effect on the steady motion. When $Pr \neq 0$, conducting boundary conditions result in more inhibition of the oscillatory motion which occurs for larger Gr than with insulating conditions; this differs from the limiting case $Pr = 0$, where the critical Grashof number at the onset of the oscillatory motion, $Gr_{c,\,osc}$, is not dependent on the thermal boundary conditions of horizontal walls.[20] The limiting case $Pr = 0$ is representative of the convective regimes for very small Pr and gives an asymptotic lower bound for the value of $Gr_{c,\,osc}$.[17] For $Pr = 0$, stability analyses predict $Gr_{c,\,osc} = 7580$ (R–F), $Gr_{c,\,osc} = 7942$ (R–R) for an infinite fluid layer[19] and $Gr_{c,\,osc} = 13\,722$ (R–F), $Gr_{c,\,osc} = 25\,525$ (R–R) for a finite cavity with an aspect ratio $A = 4$ (Table I).[20] The experimental observations of Hurle *et al.*[7] made with gallium (Pr = 0·02, R–F–A) using boats with $A \geqslant 2$ confirm the stabilizing effect of lateral walls: for $A = 4{\cdot}76$ the critical Grashof number is about 23 500 and this tends towards a limiting value of 15 000 when $A > 6$. (Herein, the insulating and conducting cases will be referred to by R–F–A, R–R–A and R–F–C, R–R–C respectively.)

In relation to the direct numerical simulation of convection in low-Pr fluids, we refer to a number of pioneering papers, for example, References 21–26. For the $A = 4$ cavity, numerical studies were conducted by the present authors with a spectral direct simulation[27,36] and by Winters using a technique which locates Hopf bifurcation conditions from a finite element solution of the extended system of equations.[28] The numerical results given in References 27, 28 and 36 agree with each other and exhibit the effect of confinement by giving a threshold at about 80% above the critical Grashof number obtained by Laure and Roux[19] for an infinite (R–F) layer with $Pr = 0$. The accurate determination of the threshold of oscillatory convection with direct simulation is very delicate because it is strongly mesh- and method-dependent. Coarse meshes may result in the stabilization of the solution and in the delay of the onset of oscillatory convection at a higher value of $Gr_{c,\,osc}$, with damped amplitudes of oscillation. Thus a wide spread is found between the critical Grashof numbers determined from the direct simulation solution, in disagreement with the results of the stability analysis. For instance, the stability analysis in a cavity of aspect ratio $A = 4$ predicts $Gr_{c,\,osc}$ at 13 722 ($Pr = 0$, R–F), 14 767 and 16 598 ($Pr = 0{\cdot}015$, R–F–C and R–F–A respectively, Table I).[28] Ben Hadid and Roux,[26] using a finite difference method, obtained $20\,000 < Gr_{c,\,osc} \leqslant 25\,000$ ($Pr = 0$, R–F) and $20\,000 < Gr_{c,\,osc} \leqslant 25\,000$ ($Pr = 0{\cdot}015$, R–F–C)*. For $Pr = 0{\cdot}015$ (R–F–A) Crochet *et al.*[24]

* Note added in proof: The critical Grashof number was overestimated by about 85 per cent as a consequence of their lack of accuracy. Following our previous results[27, 36, 50, 54] they repeated their calculations using a more accurate method and finer meshes, and finally obtained better values of $Gr_{c,\,osc}$.[55]

Table I. Summary of results concerning the critical Grashof number at the onset of time-dependent motion. Results obtained by the authors and by Winters[20]

$Pr = 0$ (present)		$Pr = 0$ (Winters[20])	
R–F $13\,100 < Gr_{c,\,osc} \leqslant 13\,500$	R–R $25\,500 < Gr_{c,\,osc} \leqslant 26\,000$	R–F 13 722	R–R 25 525
$Pr = 0{\cdot}015$ (present)		$Pr = 0{\cdot}015$ (Winters[20])	
R–F–A $18\,000 < Gr_{c,\,osc} \leqslant 19\,000$	R–R–A $33\,000 < Gr_{c,\,osc} \leqslant 33\,500$	R–F–A 16 598	R–R–A 38 085
R–F–C $14\,000 < Gr_{c,\,osc} \leqslant 14\,700$	R–R–C $28\,000 < Gr_{c,\,osc} \leqslant 28\,500$	R–F–C 14 767	R–R–C 28 153

obtained a steady solution for $Gr = 16700$ and an oscillatory one for $Gr = 79200$, but no precise investigation concerning the definite nature of the solution has been done in the intermediate range of Gr.

The high accuracy level of the numerical spectral methods should permit one to determine with more confidence the conditions of the oscillations near the threshold and the multiple supercritical solutions. One of the purposes of the present paper is to check carefully the possible effects of the spatial resolution and of the time discretization on the time behaviour of the flow solution. Thus two methods are presented for solution of the Navier–Stokes problem in the vorticity–streamfunction formulation. The methods have been detailed in previous papers: in one method the boundary conditions are handled by the influence matrix technique and the second-order backward differentiation formula/Adams–Bashforth scheme is used for integration in time;[29] in the second method the integration is made using the LSODA solver (which is based on multistep schemes) and the boundary conditions on the vorticity are evaluated explicitly.[30] The two methods (denoted I and II) are based on tau–Chebyshev approximations and are used concurrently. Our results concern numerical simulations of the flow in an $A = 4$ cavity at $Pr = 0$ (R–F and R–R) and $Pr = 0{\cdot}015$ (R–F–A, R–R–A, R–F–C and R–R–C). The main conclusion will be that the $Pr = 0$ problem is significant for a range of low-Prandtl-number situations, at least up to $Pr = 0{\cdot}015$. Identical flow regimes are encountered but with relative shifting of the thresholds.

The paper is organized as follows. In Section 2 the governing equations and associated initial and boundary conditions are formulated. The numerical methods are briefly described in Section 3. Section 4 is devoted to a general discussion of the accuracy and convergence of the solution. Finally, Section 5 is concerned with the determination and analysis of the various flow regimes.

2. PHYSICAL PROBLEM AND MODELIZATION

2.1. Governing equations

We study the behaviour of homogeneous (one-component) fluids, corresponding to a liquid metal (small Prandtl number Pr), submitted to a buoyancy force inside a rectangular cavity with a height H and a length L ($A = L/H$ is the aspect ratio). The simplified geometry adopted for the simulation is a model for the two-dimensional cross-section of a horizontal Bridgman boat. The vertical side walls of the crucible are maintained at constant temperatures T_1 and T_2 (see Figure 1). The temperature T_1 of the cold side wall is above the melting point; no growth of the crystal interface is considered and the geometry is not modified during the process. The convective flow is generated by the buoyancy force as soon as $T_1 \neq T_2$. The intensity of the resulting flow is connected to the magnitude of the difference $\delta T = T_2 - T_1 > 0$.

The bottom and side walls are rigid (no-slip and impermeability conditions) while the upper horizontal boundary is either a rigid wall (R–R case) or a free surface (stress-free and impermeability condition, R–F case). In the R–F case the liquid–gas interface is assumed to be planar. The

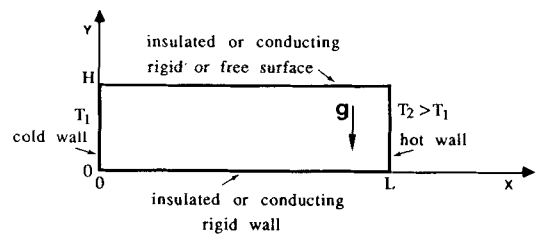

Figure 1. Geometry and boundary conditions

same conditions on the temperature are imposed at the top and bottom boundaries: either a linear variation (conducting case, denoted C) or an insulating condition (denoted A for adiabatic). The motion is assumed to be described by the Navier–Stokes equations within the Boussinesq approximation. In dimensionless variables these equations are

$$\partial\theta/\partial t + Re(\mathbf{V}\cdot\nabla\theta) = Pr^{-1}\nabla^2\theta, \tag{1}$$

$$\partial\omega/\partial t + Re(\mathbf{V}\cdot\nabla\omega) = \nabla^2\omega + Gr\,Re^{-1}\,\partial\theta/\partial x, \tag{2}$$

$$\nabla^2\psi - \omega = 0, \tag{3}$$

to be solved in the domain $0 < x < A$, $0 < y < 1$. In these equations θ is the temperature, ω the vorticity, $\mathbf{V}$ the velocity and ψ the streamfunction. The characteristic scales for space, time, velocity and temperature variables are H, H^2/ν, V^* and δT respectively. The physical dimensionless parameters are $Gr = g\alpha H^4(\delta T/L)/\nu^2$, $Re = HV^*/\nu$ and $Pr = \nu/\kappa$, where g is the gravitational acceleration, α is the thermal expansion coefficient, ν is the kinematic viscosity and κ is the thermal diffusivity.

Several choices are possible for the characteristic scale of the velocity. For instance, De Vahl Davis[31] uses $V^* = \nu/H$ (i.e. $Re = 1$) when Gr is not too large (conduction–dominated regimes); this scaling will be denoted A1. After Ostrach,[32] a suitable scaling (denoted A2) for large Gr values (when inertia terms balance buoyancy terms) corresponds to the reduced free-fall velocity $V^* = \nu Gr^{0.5}/H$ (i.e. $Re = Gr^{0.5}$). In our computations, which use these two scalings indifferently, any alterations are noted in the numerical results and the behaviour of the methods following the chosen scaling.

The dimensionless temperature is defined by $\theta = A(T - T_1)/\delta T$ and the velocity is derived from the streamfunction by $\mathbf{V} = (u, v) = (-\partial\psi/\partial y, \partial\psi/\partial x)$. In equations (1)–(3) we note that $\nabla = (\partial/\partial x, \partial/\partial y)$ and $\nabla^2 = \partial^2/\partial x^2 + \partial^2/\partial y^2$.

2.2. *Boundary conditions*

The boundary conditions ($t > 0$) on the velocity are written in terms of ψ and ω as:

on the three rigid walls $x = 0$, $x = A$ and $y = 0$,

$$\psi = \partial\psi/\partial n = 0, \tag{4}$$

where $\partial/\partial n$ denotes the normal derivative to the boundary;

on the upper horizontal boundary $y = 1$,

$$\text{either} \quad \psi = \partial\psi/\partial x = 0 \quad \text{(R–R case)} \tag{5a}$$

$$\text{or} \quad \psi = \omega = 0 \quad \text{(R–F case).} \tag{5b}$$

The boundary conditions for the temperature are:

on both side walls $x = 0$ and $x = \mathrm{A}$,

$$\theta(0, y) = 0, \qquad \theta(A, y) = A; \tag{6}$$

on the horizontal boundaries $y = 0$ and $y = 1$,

$$\text{either} \quad \partial\theta/\partial y = 0 \quad \text{(insulating condition)} \tag{7a}$$

$$\text{or} \quad \theta = x \quad \text{(conducting condition).} \tag{7b}$$

2.3. *Asymptotical solutions and starting conditions*

Simple analytical parallel steady flow solutions ($u_A(y)$, $v_A = 0$) were proposed by Hart[16, 17] for the core of long horizontal cavities when Pr is vanishing. In the limiting case $Pr = 0$ (finite ν and

infinite κ), equation (1) simplifies to

$$\nabla^2\theta = 0, \tag{8}$$

and its solution verifying the boundary conditions (6) and any of (7) is $\theta = x$, so that the buoyancy forcing term in equation (2) is constant. The velocity solution in the vertical midplane is written as

$$u_A(y) = Gr\,Re^{-1}(2y - 1)(y-1)y/12 \qquad \text{(R–R case)}, \tag{9a}$$

$$u_A(y) = Gr\,Re^{-1}(8y^2 - 15y + 6)y/48 \qquad \text{(R–F case)}. \tag{9b}$$

When $Pr \neq 0$ the temperature is expanded as $\theta = x + PrT_A(y) + \ldots$, where $Pr \ll 1$. The solution is then obtained by solving the equation resulting from (1) with the velocity solutions (9):

$$T_A(y) = Gr[y^3(6y^2 - 15y + 10) - 0{\cdot}5]/720 \qquad \text{(R–R case)}, \tag{10a}$$

$$T_A(y) = Gr[y^3(8y^2 - 25y + 20)/960 - 1/720] \qquad \text{(R–F case)} \tag{10b}$$

if the horizontal surfaces are insulating, and

$$T_A(y) = Gr[y^3(6y^2 - 15y + 10) - y]/720 \qquad \text{(R–R case)}, \tag{10c}$$

$$T_A(y) = Gr[y^3(8y^2 - 25y + 20) - 3y]/960 \qquad \text{(R–F case)} \tag{10d}$$

if the horizontal surfaces are conducting.

These analytical solutions are modified in order to match the parallel flow to the turning flow in the two end regions. Ben Hadid *et al.*[3] proposed the following relations which are used for an initial condition to start the computations:

$$\begin{aligned} u_0(x, y) &= \varepsilon(x)u_A(y), \\ v_0(x, y) &= \varepsilon'(x)\psi_A(y), \\ \omega_0(x, y) &= \varepsilon''(x)\psi_A(y) - \varepsilon(x)u'_A(y), \\ \theta_0(x, y) &= x + Pr\varepsilon(x)T_A(y), \end{aligned} \tag{11}$$

where

$$\psi_A(y) = -\int_0^y u_A(\zeta)\,d\zeta$$

and $\varepsilon(x)$ is a function introduced to ensure the no-slip conditions on the end walls $x = 0$ and $x = A$. In equations (11), u'_A, ε' and ε'' are the derivatives with respect to variables. A suitable expression for ε is

$$\varepsilon(x) = \tanh[Cx^2(A - x)^2], \quad \text{where } C = 3{\cdot}27/(A - 1)^2.$$

Various initial conditions were considered together with condition (11). Also, the motionless solution at $Gr = 0$ was used and the solution at given Gr conditions was computed by incrementing Gr progressively (either requiring or not requiring achieved convergence at each intermediate Gr step) or decrementing Gr for analysis of the hysteresis process for instance.

3. NUMERICAL SOLUTION METHOD

3.1. Space approximation

The numerical solution is obtained through the tau spectral method[33–35] using Chebyshev polynomial expansions in the two space variables. Thus each flow variable $\varphi = \{\theta, \omega, \psi\}$ is

approximated as

$$\varphi(x, y, t) = \sum_{n=0}^{N_\varphi} \sum_{m=0}^{M_\varphi} \varphi_{nm}(t)\, T_n(2x/A - 1)\, T_m(2y - 1). \tag{12}$$

Then the governing equations (1)–(3) yield

$$\mathrm{d}\theta_{nm}/\mathrm{d}t = -Re\, C_{\theta nm} + Pr^{-1} D_{\theta nm}, \tag{13}$$

$$\mathrm{d}\omega_{nm}/\mathrm{d}t = -Re\, C_{\omega nm} + D_{\omega nm} + Gr\, Re^{-1} S_{nm}, \tag{14}$$

$$D\psi_{nm} - \omega_{nm} = 0, \tag{15}$$

where $C_{\varphi nm}$, $D_{\varphi nm}$ and S_{nm} correspond to the Chebyshev polynomial expansion of C_φ, D_φ and S respectively, defined by $C_\varphi = \mathbf{V}\cdot\nabla\varphi$, $D_\varphi = \nabla^2\varphi$ and $S = \partial\theta/\partial x$. By application of the tau method, the above system is defined for $0 \leqslant n \leqslant N_\varphi - 2$ and $0 \leqslant m \leqslant M_\varphi - 2$. The complementary equations are derived from the natural boundary conditions (4)–(7). No special difficulty is encountered in enforcing the temperature conditions (6) and (7) or the stress-free condition (5b). On the other hand, for a no-slip wall the usual problem of vorticity boundary conditions arises because conditions (4) and (5a) apply to the streamfunction and its normal derivative but not to the vorticity. The determination of boundary conditions for ω is performed by means of two methods. The first (method I) is based on the influence matrix technique for determining the boundary values of ω such that the condition $\partial\psi/\partial n = 0$ is satisfied, while the second (method II) is based on the explicit evaluation of the vorticity at the boundary using equation (3) itself written at the boundary, i.e. $\omega = \partial^2\psi/\partial n^2$ in which the condition $\partial\psi/\partial n = 0$ is introduced.

Method I[29, 36] leads to a difficulty associated with the dimension of the spaces in which the approximated solution is defined. This difficulty is surmounted by considering a higher-order Chebyshev polynomial approximation to ψ and ω; that is to say, $N_\psi = N_\omega + 2 = N + 2$ and $M_\psi = M_\omega + 2 = M + 2$. For Method II, $N_\psi = N_\omega = N$ and $M_\psi = M_\omega = M$ simply.

The coefficients $C_{\varphi nm}$ coming from the non-linear terms are computed using the pseudospectral technique in which the differentiations are made in the spectral space while the products are performed in the physical space; these two spaces are connected by means of the FFT algorithm developed on the Cray vector computer by Temperton[37].

3.2. *Time discretization*

The solution is advanced in time using multistep time schemes.[38–41] Considering equations (14) and (15) in the symbolic form

$$\mathrm{d}Z/\mathrm{d}t = F(Z, t) = F_\mathrm{c} + F_\mathrm{d} + F_\mathrm{s}, \tag{16}$$

$$D\psi_{nm} - \omega_{nm} = 0, \tag{17}$$

where

$$Z = (\theta_{nm}, \omega_{nm}),$$

$$F_\mathrm{c} = (-Re\, C_{\theta nm}, -Re\, C_{\omega nm}),$$

$$F_\mathrm{d} = (Pr^{-1} D_{\theta nm}, D_{\omega nm}),$$

$$F_\mathrm{s} = (0, Gr\, Re^{-1} S_{nm}),$$

the general form of the linear multistep formula is written as

$$Z^k = \sum_{i=1}^{K_1} \alpha_i Z^{k-i} + \delta t \left[\sum_{i=0}^{K_2} \beta_i F_\mathrm{c}^{k-i} + \sum_{i=0}^{K_3} \gamma_i F_\mathrm{d}^{k-i} + \sum_{i=0}^{K_4} \eta_i F_\mathrm{s}^{k-i} \right], \tag{18}$$

$$D\psi_{nm}^{k} - \omega_{nm}^{k} = 0, \tag{19}$$

where δt is the time step and the superscript k refers to the time t^k defined by $t^k = t^{k-1} + \delta t$.

Two different schemes are considered according to the processing of the boundary conditions. The first (method I) is semi-implicit and composed of a combination of the second-order backward differentiation formula (BDF scheme) and an Adams–Bashforth-type scheme. The scheme is expressed with $K_1 = K_2 = 2$, $K_3 = K_4 = 0$; $\alpha_1 = 4/3$, $\alpha_2 = -1/3$; $\beta_0 = 0$, $\beta_1 = 4/3$, $\beta_2 = -2/3$; $\gamma_0 = \eta_0 = 2/3$. Thus we obtain the equation

$$(3Z^k - 4Z^{k-1} + Z^{k-2})/2\delta t = 2F_c^{k-1} - F_c^{k-2} + F_d^k + F_s^k, \tag{20}$$

which is second-order accurate in time. The good stability properties of the scheme have been exhibited in Ouazzani *et al.*[42] for the advection–diffusion equation and in Ehrenstein[43] and Ehrenstein and Peyret[44] for the Stokes and Navier–Stokes equations. This scheme leads to the solution of a Helmholtz equation for θ^k with the boundary conditions (6) and (7). Then the known value of θ^k is brought into the equation for ω^k, giving a Stokes-type problem for (ω^k, ψ^k) with the boundary conditions (4) and (5). This problem is solved by means of an influence matrix technique,[29] leading to the solution of successive Helmholtz and Poisson equations with Dirichlet boundary conditions. All these equations (for θ^k, ω^k and ψ^k) are solved by means of the matrix diagonalization technique.[45]

The second scheme used in method II[30] is based on the ODE solver LSODA which includes both a selection of schemes and an automatic adaptation of the time step according to the level of stiffness of the problem.[39–41] During the transient, the Adams–Moulton scheme (denoted AM) is used:

$$Z^k = Z^{k-1} + \delta t \sum_{i=0}^{q-1} \beta_i F^{k-i};$$

this corresponds to $K_1 = 1$ and $K_2 = q - 1$, where the integer q is the accuracy order[38] and the coefficients β_i ($\beta_0 > 0$) depend on q (with $1 \leqslant q \leqslant 12$). Beyond the transient, the LSODA code switches to the BDF scheme, where $K_1 = q$ and $K_2 = 0$:

$$Z^k = \sum_{i=1}^{q} \alpha_i Z^{k-i} + \delta t \beta_0 F^k,$$

with $1 \leqslant q \leqslant 5$. When $q = 2$ the BDF scheme corresponds to the aforementioned second-order scheme used for the linear part in equation (20). The LSODA solver is used for each δt increment as given in Tables II and III ($10^{-4} < \delta t < 10^{-1}$) and the solution is determined within an absolute error corresponding to the tolerance parameter r which governs the local time step for each scheme. In the range of solutions presented, r was varied from 10^{-1} to 10^{-6}.

4. COMPUTATIONAL ASPECTS

4.1. Numerical features

The computations, carried out on a Cray2, were generally performed in the R–F case with both method I and scaling A2, and method II and scaling A1, and in the R–R case with method I and scaling A2. However, for convenience of comparison, all results presented in forthcoming sections are scaled with A2. In particular, a number of characteristic variables defined as follows will be discussed: ψ_{max}, the maximum value of ψ in the steady state solutions or at given instants in the oscillatory solutions; ψ_{mid}, the value of ψ at the midpoint ($x = A/2$, $y = 1/2$); ψ_{quart}, the value

of ψ at ($x = A/4$, $y = 1/4$); Res-ω, the residual on ω, Res-$\omega = (\mathrm{Sup}|\vartheta^k - \vartheta^{k-1}|)/(\delta t\ \mathrm{Sup}|\vartheta^k|)$, where ϑ corresponds to the spectral coefficient of ω for method I and to the value of ω at collocation points for method II; $t_f - t_i$, the time interval for integration; f, the fundamental dimensionless frequency of the oscillations; $\psi_{max,\,max}$, the maximum value of the time history of ψ_{max}; $\psi_{max,\,min}$, the minimum value of the time history of ψ_{max}; $\psi_{max,\,mean}$, the average value of ψ_{max}, $\psi_{max,\,mean} = (\psi_{max,\,max} + \psi_{max,\,min})/2$; $\psi_{max,\,f}$, the amplitude of oscillations of ψ_{max}, $\psi_{max,\,f} = (\psi_{max,\,max} - \psi_{max,\,min})/\psi_{max,\,mean}$.

The details of the computations are given in Tables II–VII. The results are focused on the accurate prediction of the onset of oscillatory regimes in both R–R and R–F cases. The supercritical oscillatory regimes are simulated for $Pr = 0$ and 0·015. The stability of the solutions was studied with respect to different kinds of initial conditions and disturbances. For each value of Gr the initial condition is given either by the asymptotic solution (11) or by a solution already obtained at a smaller or larger value of Gr. The last two columns in the tables refer to the initial condition and specify the type of solution obtained respectively. The fundamental frequency f given in the tables is calculated in most cases by simply measuring the time difference separating the maxima of ψ_{max}. In a limited number of cases a power spectrum analysis was performed on the time history of ψ_{mid} and ψ_{quart} (see following Figure 18).

For method I the value of the time step δt varies from 4×10^{-5} to 2×10^{-4} according to Gr and to the resolution (see Tables II–VII). The stability imposes δt values much smaller (one-thousandth) than the period of the oscillations, which ensures the time accuracy of the results. On a Cray2 computer, the computational cost for one time step is 0·01 s for $Pr = 0$ with spatial resolution defined by $N = N_\omega = N_\psi - 2 = 30$ and $M = M_\omega = M_\psi - 2 = 16$, and 0·024 s with $N = 40$ and $M = 30$; these times are increased by about 30% when the temperature equation is solved. With method II the LSODA solver switches rapidly from the AM ($q = 2$) scheme to the BDF ($q = 1$–2) scheme after a very short transient compared to the establishment of the steady or oscillatory state. In some steady cases large δt values were used in order to accelerate the convergence. The CPU time costs are approximately 0·09–0·30 s for the computations corresponding to a time interval of 4×10^{-4} with $N = N_\omega = N_\psi = 27$ and $M = M_\omega = M_\psi = 15$ for a tolerance parameter $r = 10^{-1}$–10^{-2}. The cost for one period at near-critical conditions is approximately 18–36 s, i.e. at least twice the cost with method I for a similar resolution.

4.2. Convergence towards steady state solutions

For steady state solutions the integration process is stopped when the residual decays below a required value, Res-$\omega < 10^{-4}$ with method II (see Table II). On the other hand, some calculations devoted only to determine the final (steady or time-dependent) behaviour of the solution were stopped with much larger residuals. (In such cases the values of ψ_{max} given in the tables might be somewhat inaccurate). In the R–F case and for $Pr = 0$ the time increment can be taken as large as $\delta t = 0{\cdot}1$ for 20×12 resolution with method II ($r = 10^{-3}$) and at most $\delta t = 2 \times 10^{-4}$ for 30×16 in the case of method I. Steady state solutions have been obtained up to $Gr = 13\,100$ when using initial conditions corresponding to either a zero-velocity field or to the asymptotic solution (11) or by incrementing Gr progressively. For example, at $Gr = 12\,750$ the improvement of accuracy (by increasing the resolution; see Table II) is associated to a reduced convergence rate. Thus, with method II and with the initial guess derived from the solution obtained with a small number of polynomials, the residual decays to only about 10^{-4} with $\delta t = 0{\cdot}1$ after $150\delta t$ for 32×15. In comparison, it reaches about 10^{-8} after $160\delta t$ with 20×12.

In the R–R case with $Pr = 0$, Gresho and Sani,[46] Roux *et* al.[47] and Ben Hadid *et al.*[3] have observed interesting features of the solution when $Gr = 5 \times 10^4$. First the solution is regularly

Table II. List of runs in the R–F case for $Pr = 0$

Gr	Method	$N \times M$	δt (r)	$\psi_{max,\,mean}$	$\psi_{max,\,f}$ (%)	f	Res-ω	$t_f - t_i$	Initial condition	Type of solution
117	II	20 × 12	10^{-1} (10^{-3})	0·058	—	—	10^{-7}	1·2	$Gr = 78$ (20 × 12)	S1
3124	II	20 × 12	10^{-1} (10^{-3})	0·318	—	—	10^{-5}	2·2	$Gr = 1562$ (20 × 12)	S1
10000	II	20 × 12	10^{-1} (10^{-3})	0·5469	—	—	10^{-5}	0·9	$Gr = 7800$ (20 × 12)	S11
	I	30 × 16	2×10^{-4}	0·5500	—	—	8×10^{-3}	0·9	Sol. (11)	S11
	I	30 × 24	$1·5 \times 10^{-4}$	0·5500	—	—	8×10^{-6}	3	Sol. (11)	S11
12750	II	20 × 12	10^{-1} (10^{-3})	0·5932	—	—	8×10^{-9}	16	$Gr = 11250$ (20 × 12)	S11
	II	24 × 12	10^{-1} (10^{-3})	0·5939	—	—	8×10^{-9}	2·8	$Gr = 12750$ (20 × 12)	S11
	II	24 × 15	10^{-1} (10^{-3})	0·5927	—	—	10^{-7}	8	$Gr = 12750$ (24 × 12)	S11
	II	27 × 15	10^{-1} (10^{-3}–10^{-5})	0·5978	—	—	10^{-5}	20	$Gr = 12750$ (24 × 15)	S11
	II	32 × 15	10^{-1} (10^{-3})	0·5976	—	—	2×10^{-4}	15	$Gr = 12750$ (27 × 15)	S11
13000	I	30 × 24	10^{-4}	0·6000	—	—	0·411†	4	Sol. (11)	S11
13500	II	27 × 15	4×10^{-3}–2×10^{-2} (10^{-4}–10^{-6})	0·6085*	0·54	12·32	—	2·89	$Gr = 13100$ (27 × 15)	P1
	II	27 × 15	2×10^{-3} (10^{-2}–10^{-4})	0·6072*	2·70	12·20	—	1·19	$Gr = 15000$ (27 × 15)	P1
	II	27 × 15	4×10^{-4}–2×10^{-3} (10^{-1}–10^{-2})	0·6078*	1·92	12·32	—	3·16	$Gr = 0$ (rest)	P1
	I	30 × 16	10^{-4}	0·6030*	3·91	12·15	—	5	Sol. (11)	P1
	II	32 × 16	4×10^{-4} (10^{-4})	0·6008*	3·25	12·37	—	2·32	$Gr = 13500$ (27 × 15)	P1
	I	30 × 24	10^{-4}	0·6048*	3·93	12·46	—	8·5	$Gr = 13000$ (30 × 24)	P1
15000	II	20 × 12	4×10^{-4}–4×10^{-2} (10^{-4}–10^{-6})	0·6234*	0·14	≈14	—	0·54	$Gr = 14000$ (20 × 12)	P1
	II	25 × 15	2×10^{-3}–4×10^{-2} (10^{-3})	0·6170*	8·05	≈14	—	0·65	$Gr = 14000$ (20 × 12)	P1
	II	27 × 15	4×10^{-4}–2×10^{-3} (10^{-4}–10^{-7})	0·6130*	9·57	13·05	—	2·37	$Gr = 14500$ (27 × 15)	P1
	II	30 × 16	4×10^{-4} (10^{-4})	0·6070*	10·89	12·93	—	6·60	$Gr = 15000$ (32 × 16)	P1
	I	30 × 16	10^{-4}	0·6060*	10·89	13·04	—	4	Sol. (11)	P1
	I	30 × 24	10^{-4}	0·6090*	10·80	13·04	—	4·4	$Gr = 13500$ (30 × 24)	P1
	II	32 × 16	4×10^{-4} (10^{-4})	0·6110*	8·93	13·23	—	4	$Gr = 13500$ (32 × 16)	P1
	II	32 × 20	2×10^{-4} (10^{-1})	0·6111*	9·10	13·27	—	12	$Gr = 15000$ (32 × 16)	P1
	II	48 × 20	2×10^{-4} (10^{-1})	0·6119*	9·03	13·31	—	7·4	$Gr = 15000$ (32 × 20)	P1
17500	II	27 × 15	4×10^{-4}–4×10^{-3} (10^{-4}–10^{-5})	0·6142*	19·08	14·01	—	1·00	$Gr = 15000$ (27 × 15)	P1
20000	II	27 × 15	4×10^{-4}–2×10^{-3} (10^{-2})	0·6233*	21·20	15·70	—	0·37	$Gr = 17500$ (27 × 15)	P1
	I	30 × 16	10^{-4}‡	0·6310*	17·54	16·18	—	4·02	Sol. (11)	P1
	I	30 × 24	10^{-4}	0·6330*	18·0	16·20	—	4·3	$Gr = 15000$ (30 × 24)	P1
	II	32 × 16	4×10^{-4} (10^{-4})	0·6254*	18·56	16·05	—	3·30	$Gr = 15000$ (32 × 16)	P1
	II	48 × 20	2×10^{-4} (10^{-1})	0·6309*	17·03	16·12	—	5·68	$Gr = 15000$ (48 × 20)	P1
25000	II	32 × 16	4×10^{-4} (10^{-4})	0·6476*	20·70	18·87	—	1·63	$Gr = 20000$ (32 × 16)	P1
30000	I	30 × 16	5×10^{-5}	0·6680*	22·43	21·39	—	3	$Gr = 20000$ (30 × 16)	P1
	II	32 × 16	4×10^{-4} (10^{-4})	0·6749*	20·33	21·06	—	1·62	$Gr = 25000$ (32 × 16)	P1
	II	48 × 20	2×10^{-4} (10^{-1})	0·5999*	23·92	21·19	—	2·43	$Gr = 20000$ (48 × 20)	P1

* Oscillatory mean value.
† Slow tendency to converge.
‡ $\delta t = 5 \times 10^{-5}$ up to $t = 0·02$ and $\delta t = 10^{-4}$ after this time.

Table III. List of runs in the R–R case for $Pr = 0$

Gr	Method	$N \times M$	δt	$\psi_{max,\,mean}$	$\psi_{max,\,f}$ (%)	f	Res-ω	$t_f - t_i$	Initial condition	Type of solution
10000	I	30 × 16	2×10^{-4}	0·3109	—	—	10^{-8}	0·76	Sol. (11)	S1
20000(a)	I	30 × 16	2×10^{-4}	0·4154	—	—	$2{\cdot}5 \times 10^{-6}$	1·5	Sol. (11)	S12
(b)	I	30 × 16	2×10^{-4}	0·4154	—	—	$4{\cdot}26 \times 10^{-5}$	1·2	Gr = 10000	S12
(c)	I	30 × 20	2×10^{-4}	0·4155	—	—	$6{\cdot}27 \times 10^{-8}$	2	Sol. (11)	S12
(d)	I	40 × 30	1×10^{-4}	0·4155	—	—	$5{\cdot}69 \times 10^{-6}$	2	Gr = 25000(d) (40 × 30)	S12
24000	I	40 × 30	1×10^{-4}	0·4400	—	—	$1{\cdot}26 \times 10^{-6}$	4	Gr = 24500 (40 × 30)	S12
24500	I	40 × 30	1×10^{-4}	0·3683	—	—	$3{\cdot}53 \times 10^{-6}$	4	Gr = 25000(d) (40 × 30)	S2
25000(a)	I	30 × 16	2×10^{-4}	0·4453	—	—	7×10^{-3}	4	Sol. (11)	S12
(b)	I	30 × 20	2×10^{-4}	0·4453	—	—	$4{\cdot}59 \times 10^{-3}$	4	Sol. (11)	S12
(c)	I	40 × 30	1×10^{-4}	0·4452	—	—	1·34	2	Gr = 30000(c) (40 × 30)	S12
(d)	I	40 × 30	1×10^{-4}	0·3676	—	—	$1{\cdot}90 \times 10^{-6}$	4	Gr = 26000(b) (40 × 30)	S2
25500	I	40 × 30	1×10^{-4}	0·4480	—	—	1·05	2	Gr = 25000(c) (40 × 30)	S12
26000(a)	I	40 × 30	1×10^{-4}	0·4504*	3·28	16·31	—	6·2	Gr = 25500 (40 × 30)	P1
(b)	I	40 × 30	1×10^{-4}	0·3682	—	—	$2{\cdot}44 \times 10^{-6}$	2	Gr = 30000(e) (40 × 30)	S2
26500	I	30 × 16	2×10^{-4}	0·4528*	2·82	17·12	—	4	Sol. (11)	P1
27500	I	30 × 16	2×10^{-4}	0·4567*	5·32	17·6	—	4	Gr = 25000(a) (30 × 16)	P1
28500	I	40 × 30	1×10^{-4}§	0·4601*	7·66	17·3	—	4·35	Sol. (11)	P1
29500	I	40 × 30	1×10^{-4}	0·4587*	10·99	17·45	—	13·7	Gr = 28500 (40 × 30)	QP
30000(a)	I	30 × 16	2×10^{-4}	0·4567*	12·2	17·43	—	4·4	Gr = 20000(b) (30 × 16)	QP
(b)	I	30 × 16	2×10^{-4}‡	0·4567*	12·2	17·43	—	4·1	Sol. (11)	QP
	II	30 × 16	4×10^{-4}†	0·4540*	13·5	17·46	—	5·6	Gr = 0 (rest)	QP
	II	30 × 16	4×10^{-4}†	0·4540*	13·5	17·46	—	2	Gr = 25000	QP
(c)	I	40 × 30	1×10^{-4}	0·4587*	12·0	17·55	—	12·1	Gr = 30000(b) (30 × 16)	QP
(d)	I	40 × 30	1×10^{-4}	0·4587*	12·0	17·55	—	8	Gr = 25500 (40 × 30)	QP
(e)	I	40 × 30	1×10^{-4}	0·3841	—	—	$4{\cdot}30 \times 10^{-6}$	4	Gr = 31000(b) (40 × 30)	S2
(f)	I	40 × 30	1×10^{-4}	0·3841	—	—	1.50×10^{-6}	4	Gr = 25000(d) (40 × 30)	S2
(g)	I	60 × 60	5×10^{-5}	0·4624*	10·6	17·63	—	13·1	Gr = 30000(c) (40 × 30)	QP
(h)	I	80 × 60	5×10^{-5}	0·4632*	9·80	17·63	—	12	Gr = 30000(d) (40 × 30)	QP
(i)	I	90 × 80	$2{\cdot}5 \times 10^{-5}$	0·4632*	9·80	17·63	—	11	Gr = 30000(d) (40 × 30)	QP
(j)	I	100 × 80	$2{\cdot}5 \times 10^{-5}$	0·4632*	9·80	17·63	—	13·5	Gr = 30000(i) (90 × 80)	QP
30100	I	40 × 30	1×10^{-4}	0·4553*	13·3	17·56	—	4	Gr = 30000(d) (40 × 30)	QP
30300	I	40 × 30	1×10^{-4}	0·4552*	14·4	17·52	—	4	Gr = 30100 (40 × 30)	QP
30400	I	40 × 30	1×10^{-4}	0·4537*	15·0	17·53	—	8	Gr = 30300 (40 × 30)	QP
30450	I	40 × 30	1×10^{-4}	0·4535*	15·6	17·50	—	8	Gr = 30400 (40 × 30)	QP
30500	I	40 × 30	1×10^{-4}	0·4617*	10·44	17·33	—	8	Gr = 30450 (40 × 30)	P2
31000(a)	I	40 × 30	1×10^{-4}	0·4619*	9·84	17·12	—	3·3	Gr = 30000(c) (40 × 30)	P2
(b)	I	40 × 30	1×10^{-4}	0·3877	—	—	$1{\cdot}13 \times 10^{-6}$	4	Gr = 35000 (40 × 30)	S2
32000	I	40 × 30	1×10^{-4}	0·4391*	20·2	16·45	—	4·3	Gr = 30500 (40 × 30)	P2
33000	I	40 × 30	1×10^{-4}	0·4285*	24·9	16·45	—	4·3	Gr = 32000 (40 × 30)	P2
33500	I	40 × 30	1×10^{-4}	0·3960	—	—	$4{\cdot}29 \times 10^{-7}$	4	Gr = 30500 (40 × 30)	S2
34000	I	40 × 30	1×10^{-4}	0·3976	—	—	$1{\cdot}45 \times 10^{-6}$	4·3	Gr = 33000 (40 × 30)	S2
35000	I	40 × 30	1×10^{-4}§	0·4007	—	—	$2{\cdot}39 \times 10^{-6}$	2·5	Sol. (11)	S2
40000(a)	I	30 × 16	1×10^{-4}	0·4092	—	—	10^{-8}	2·85	Sol. (11)	S2
(b)	I	40 × 30	$7{\cdot}5 \times 10^{-5}$	0·4151	—	—	$1{\cdot}68 \times 10^{-6}$	3	Gr = 35000 (40 × 30)	S2
50000(a)	I	40 × 16	1×10^{-4}§	0·4401	—	—	7×10^{-4}	1·13	Sol. (11)	S2
(b)	I	50 × 30	4×10^{-5}	0·4392	—	—	$1{\cdot}2 \times 10^{-6}$	2	Sol. (11)	S2

* Oscillatory mean value. ‡ $\delta t = 10^{-4}$ up to $t = 0{\cdot}1$ and $\delta t = 2 \times 10^{-4}$ after this time.
† Method II ($r = 10^{-1}$). § $\delta t = 5 \times 10^{-5}$ up to $t = 0{\cdot}02$ and $\delta t = 1 \times 10^{-4}$ after this time.

Table IV. List of runs in the R–F–A case for $Pr = 0{\cdot}015$ (method I)

Gr	$N \times M$	δt	$\psi_{max,\,mean}$	$\psi_{max,\,f}$ (%)	f	Res-ω	$t_t - t_i$	Initial condition	Type of solution
10000(a)	30 × 16	2×10^{-4}	0·5300	—	—	$1{\cdot}24 \times 10^{-3}$	0·7	Sol. (11)	S11
(b)	36 × 30	1×10^{-4}	0·5350	—	—	$2{\cdot}69 \times 10^{-2}$	0·5	Sol. (11)	S11
15000(a)	30 × 16	1×10^{-4}	0·5900	—	—	$1{\cdot}99 \times 10^{-2}$	1·05	Sol. (11)	S11
(b)	36 × 30	1×10^{-4}	0·5960	—	—	0·812	0·1	Gr = 10000(b) (36 × 30)	S11
(c)	40 × 30	1×10^{-4}†	0·5940	—	—	$1{\cdot}18 \times 10^{-4}$	2·05	Sol. (11)	S11
17000(a)	36 × 30	1×10^{-4}	0·6110	—	—	$1{\cdot}55 \times 10^{-2}$	1·5	Gr = 15000(b) (36 × 30)	S11
(b)	40 × 30	1×10^{-4}	0·6100	—	—	$1{\cdot}03 \times 10^{-2}$	1·5	Gr = 15000(c) (40 × 30)	S11
18000(a)	36 × 30	$7{\cdot}5 \times 10^{-5}$	0·6180	—	—	$3{\cdot}66 \times 10^{-2}$	1·5	Gr = 17000(a) (36 × 30)	S11
(b)	40 × 30	$7{\cdot}5 \times 10^{-5}$	0·6170	—	—	$5{\cdot}82 \times 10^{-2}$	1·12	Gr = 17000(b) (40 × 30)	S11
18500	40 × 30	$7{\cdot}5 \times 10^{-5}$	0·6200	—	—	$8{\cdot}64 \times 10^{-2}$	1·12	Gr = 18000(b) (40 × 30)	S11
19000(a)	30 × 16	1×10^{-4}	0·6210	—	—	$1{\cdot}53 \times 10^{-2}$	4·9	Gr = 15000(a) (30 × 16)	S11
(b)	36 × 30	$7{\cdot}5 \times 10^{-5}$	0·6230*	2·12	14·91	—	11·4	Gr = 18000(a) (36 × 30)	P1
20000	30 × 16	1×10^{-4}	0·6190*	5·94	15·4	—	4·9	Gr = 15000(a) (30 × 16)	P1
30000(a)	30 × 16	1×10^{-4}†	0·6340*	13·03	20·16	—	4·025	Sol. (11)	P1
(b)	40 × 30	5×10^{-5}	0·6380*	12·63	20·08	—	2·2	Gr = 18500 (40 × 30)	P1
40000	30 × 16	5×10^{-5}	0·6470*	14·37	24·93	—	3	Gr = 30000(a) (30 × 16)	P1

* Oscillatory mean value.
† $\delta t = 5 \times 10^{-5}$ up to $t = 0{\cdot}025$ and $\delta t = 1 \times 10^{-4}$ after this time.

Table V. List of runs in the R–F–C case for $Pr = 0{\cdot}015$ (method I)

Gr	$N \times M$	δt	$\psi_{max,\,mean}$	$\psi_{max,\,f}$ (%)	f	Res-ω	$t_f - t_i$	Initial condition	Type of solution
10000	30 × 24	1×10^{-4}	0·5460	—	—	$5{\cdot}85 \times 10^{-4}$	1	Sol. (11)	S11
13000	30 × 24	1×10^{-4}	0·5920	—	—	0·31	1	Sol. (11)	S11
14000	30 × 24	1×10^{-4}	0·6050	—	—	$6{\cdot}56 \times 10^{-3}$	4	Sol. (11)	S11
14700	30 × 24	1×10^{-4}	0·6110*	4·1	13·07	—	8·3	$Gr = 14000$ (30 × 24)	P1
15000	30 × 24	1×10^{-4}	0·6120*	5·7	13·08	—	5·3	$Gr = 14700$ (30 × 24)	P1
20000	30 × 24	1×10^{-4}	0·6230*	15·8	15·94	—	5·3	$Gr = 15000$ (30 × 24)	P1

* Oscillatory mean value.

Table VI. List of runs in the R–R–A case for $Pr = 0{\cdot}015$ (method I)

Gr	$N \times M$	δt	$\psi_{max,\,mean}$	$\psi_{max,\,f}$ (%)	f	Res-ω	$t_f - t_i$	Initial condition	Type of solution
20000	30 × 16	2×10^{-4}	0·3944	—	—	10^{-8}	1·07	Sol. (11)	S12
25000	30 × 16	2×10^{-4}	0·4159	—	—	10^{-8}	1·65	$Gr = 20000$ (30 × 16)	S12
30000	30 × 16	2×10^{-4}	0·4315	—	—	$4{\cdot}1 \times 10^{-4}$	2	$Gr = 25000$ (30 × 16)	S12
32500	30 × 16	2×10^{-4}	0·4378	—	—	$3{\cdot}3 \times 10^{-2}$†	4	$Gr = 30000$ (30 × 16)	S12
33000	40 × 30	1×10^{-4}	0·4384	—	—	4·4†	6·4	Sol. (11)	S12
33500	40 × 30	1×10^{-4}	0·4393*	3·35	19·72	—	4·3	$Gr = 33000$ (40 × 30)	P1
35000	30 × 16	2×10^{-4}	0·4421*	4·93	20·32	—	4	$Gr = 32500$ (30 × 16)	P1
37500	30 × 16	2×10^{-4}	0·4455*	7·91	21·36	—	4	$Gr = 35000$, $t = 4$ (30 × 16)	P1
40000(a)	30 × 16	2×10^{-4}	0·4487*	10·04	22·42	—	4	$Gr = 37500$, $t = 4$ (30 × 16)	P1
(b)	40 × 30	1×10^{-4}	0·4486*	10·92	21·88	—	4·3	$Gr = 33000$, $t = 2{\cdot}4$ (40 × 30)	P1

* Oscillatory mean value.
† Slow tendency to converge.

Table VII. List of runs in the R–R–C case for $Pr = 0{\cdot}015$ (method I)

Gr	$N \times M$	δt	$\psi_{max,\,mean}$	$\psi_{max,\,f}$ (%)	f	Res-ω	$t_f - t_i$	Initial condition	Type of solution
20000	30 × 16	2×10^{-4}	0·4074	—	—	10^{-8}	1·48	Sol. (11)	S12
25000	30 × 16	2×10^{-4}	0·4337	—	—	$6{\cdot}52 \times 10^{-8}$	3	$Gr = 20000$, $t = 1{\cdot}48$ (30 × 16)	S12
27000	30 × 24	$1{\cdot}5 \times 10^{-4}$	0·4427	—	—	$8{\cdot}43 \times 10^{-5}$	3	$Gr = 25000$, $t = 3$ (30 × 16)	S12
28000	30 × 24	$1{\cdot}5 \times 10^{-4}$	0·4469	—	—	$7{\cdot}99 \times 10^{-2}$	3	$Gr = 27000$, $t = 3$ (30 × 24)	S12
28500(a)	30 × 24	$1{\cdot}5 \times 10^{-4}$	0·4489	—	—	$8{\cdot}12 \times 10^{-3}$	3	$Gr = 28000$, $t = 3$ (30 × 24)	S12
(b)	40 × 30	1×10^{-4}	0·4487*	2·59	17·45	—	15·3	$Gr = 28500$, $t = 3$ (30 × 24)	P1
30000(a)	30 × 24	$1{\cdot}5 \times 10^{-4}$	0·4539*	3·92	18·40	—	6·45	$Gr = 28500$, $t = 3$ (30 × 24)	P1
(b)	40 × 30	1×10^{-4}†	0·4532*	5·78	18·02	—	4·1	Sol. (11)	P1
35000(a)	30 × 16	$1{\cdot}5 \times 10^{-4}$	0·4634*	10·82	19·85	—	18·6	Sol. (11)	QP
(b)	40 × 30	1×10^{-4}	0·4673*	10·06	20·04	—	8·8	$Gr = 30000$(b), $t = 4{\cdot}1$ (40 × 30)	P1
35500	30 × 16	$1{\cdot}5 \times 10^{-4}$	0·4645*	11·30	19·91	—	9	$Gr = 35000$(a), $t = 15$ (30 × 16)	QP
36000	30 × 16	$1{\cdot}5 \times 10^{-4}$	0·4648*	12·11	20·01	—	9	$Gr = 35500$, $t = 9$ (30 × 16)	QP
36500	30 × 16	$1{\cdot}5 \times 10^{-4}$	0·4652*	12·81	20·14	—	9	$Gr = 36000$, $t = 9$ (30 × 16)	QP
37000	30 × 16	$1{\cdot}5 \times 10^{-4}$	0·4687*	11·88	20·29	—	9	$Gr = 36500$, $t = 9$ (30 × 16)	QP
37500(a)	30 × 16	$1{\cdot}5 \times 10^{-4}$‡	0·4654*	13·54	19·72	—	7	Sol. (11)	P2
(b)	30 × 16	$1{\cdot}5 \times 10^{-4}$	0·4654*	13·54	19·72	—	9	$Gr = 37000$, $t = 9$ (30 × 16)	P2
(c)	40 × 30	1×10^{-4}	0·4739*	11·15	21·00	—	8·4	$Gr = 35000$(b), $t = 8{\cdot}8$ (40 × 30)	P1
38000	40 × 30	1×10^{-4}	0·4693*	10·63	19·88	—	21	$Gr = 37500$(c), $t = 8{\cdot}4$ (40 × 30)	P2
38500	40 × 30	$7{\cdot}5 \times 10^{-5}$§	0·4700*	10·32	19·9	—	15·9	$Gr = 37500$(c), $t = 8{\cdot}4$ (40 × 30)	P2
39000	40 × 30	$7{\cdot}5 \times 10^{-5}$	0·4708*	9·99	19·93	—	3·75	$Gr = 38500$, $t = 15{\cdot}9$ (40 × 30)	P2
40000(a)	30 × 24	1×10^{-4}	0·4686*	14·61	20·28	—	4	$Gr = 28500$, $t = 3$ (30 × 24)	P2
(b)	40 × 30	$7{\cdot}5 \times 10^{-5}$	0·4743*	11·56	19·80	—	7	$Gr = 40000$(a), $t = 4$ (30 × 24)	P2
(c)	90 × 80	$2{\cdot}5 \times 10^{-5}$	0·4734*	12·26	19·62	—	8·45	$Gr = 40000$(b), $t = 7$ (40 × 30)	P2
45000	40 × 30	$7{\cdot}5 \times 10^{-5}$	0·4107	–	—	$9{\cdot}5 \times 10^{-6}$	3·05	Sol. (11)	S2

* Oscillatory mean value.
† $\delta t = 5 \times 10^{-5}$ up to $t = 0{\cdot}1$ and $\delta t = 10^{-4}$ after this time.
‡ $\delta t = 10^{-4}$ up to $t = 0{\cdot}4$ and $\delta t = 1{\cdot}5 \times 10^{-4}$ after this time.
§ $\delta t = 10^{-4}$ up to $t = 8{\cdot}4$ and $\delta t = 7{\cdot}5 \times 10^{-5}$ after this time.

oscillating over a large number of cycles; then it changes, to tend ultimately towards a steady solution. Roux *et al.*[47] made use of a pseudo-unsteady method while Gresho and Sani[46] and Ben Hadid *et al.*[3] used a true unsteady method. Roux *et al.* and Ben Hadid *et al.* reported that they obtained the steady state by adding an asymmetric disturbance to the initial condition (11).

With method I we obtained a steady solution using the initial condition (11) at $Gr = 5 \times 10^4$ after a short transient stage of nine and six oscillations respectively corresponding to 50×30 and 40×16 resolutions (Figures 2(a) and 2(b)). We observed that the convergence to the steady state is accelerated when disturbing the 50×30 solution by a 50% increase of the instantaneous value of ψ ($x = A/4$, $y = 1/4$) at some instants (as indicated by arrows in Figure 2(c)). In this calculation the steady solution is obtained after only four oscillations. Such a behaviour suggests that the oscillating solution is weakly unstable. Reverse transitions towards the steady state will be discussed again later.

4.3. Accuracy

The accuracy is first studied for $Pr = 0$ and the R–F case (Table II): the space accuracy is discussed at $Gr = 10\,000$ and $12\,750$, below the onset of oscillations, and the time accuracy is discussed for supercritical conditions at $Gr = 13\,500$, $15\,000$ and $17\,500$. The influence of the space accuracy on the onset of oscillations is emphasized also at critical conditions for $Pr = 0{\cdot}015$ in the R–F–A (Table IV) and R–R–C (Table VII) cases. The accuracy is also concerned in the R–R

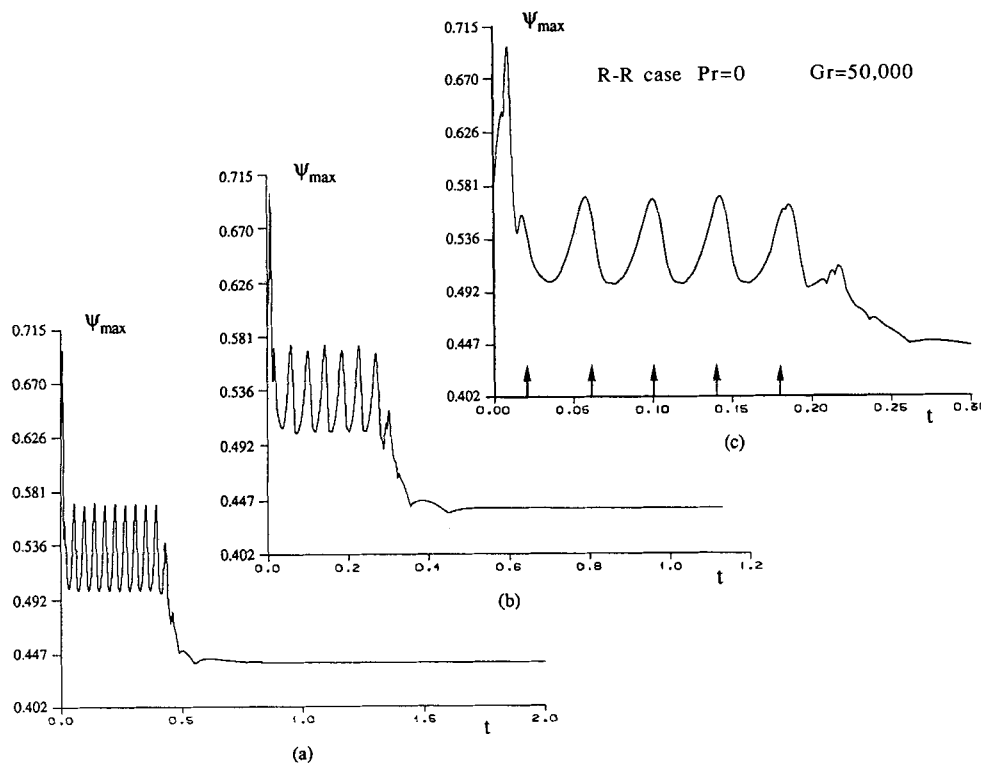

Figure 2. Effect of mode number and influence of a dynamical disturbance on the convergence to steady solution at $Gr = 50\,000$ in the R–R case for $Pr = 0$ (method I, scaling A1): (a) 50×30 solution; (b) 40×16 solution; (c) 50×30 solution and disturbances at distinct times indicated by vertical arrows in the time history of ψ_{max}

case when a second frequency appears in the solution (Table III), but this will be discussed in Section 5.2.2 in the perspective of the study of quasi-periodic motion.

At $Gr = 10000$ (R–F) the values of ψ_{max} at steady state obtained with method I (30 × 16) and method II (20 × 12) differ only by 0·6%, while the difference is about 2% when they are compared with a 61 × 31 finite difference solution.[26] Again at $Gr = 12750$ the solutions computed with method II using 20 × 12 to 32 × 15 resolutions differ by 0·7% on ψ_{max}. The influence of the tolerance parameter r in method II was tested for time-dependent solutions at $Gr = 13500$ and 17 500 when starting from the same initial condition: after several periods the differences are evaluated as only 0·01% to 0·001% on variable ψ_{max} when r varies between 5×10^{-1} and 10^{-4} The fluctuation rate $\psi_{max,f}$ is represented in Figure 3 for $Gr = 15000$ when the resolution is improved from 20 × 12 to 48 × 20 and using both methods I and II (Table II). For low resolution $\psi_{max,f}$ increases rapidly with the degree of the polynomial approximation. For resolution higher than 30 × 16 this amplitude reaches an asymptotic value of nearly 9%. Recent finite difference computations with the method used by Ben Hadid and Roux[26] based on a regular 121 × 31 mesh have given $\psi_{max,f} = 8{\cdot}37\%$, $\psi_{max,mean} = 0{\cdot}6193$ and $f = 13{\cdot}19$, which tend to agree with our solution.

The precise determination of the threshold depends mainly on the spatial accuracy of the solution. With a 20 × 12 resolution an oscillatory behaviour is observed at $Gr = 15000$ while the solution is steady at $Gr = 14500$. The onset is obtained at $Gr = 13500$ with 27 × 15. For $Gr = 13500$ the oscillations establish very slowly and the transient depends strongly on the initial condition. When starting from the steady solution at $Gr = 13100$ the amplitude still remains very small with 27 × 15 after a relatively large integration time. On the other hand, the final amplitude (about 4%) can be obtained at $t = 5$ starting from solution (11) and with 30 × 16. (See further discussion in Section 5.1.2.) The transient towards the oscillatory solution is shown to shorten when Gr is increased above the critical Gr (see Figure 8). The effect of the spatial resolution on the onset of oscillations is emphasized in the R–R–C case at $Gr = 28500$ (Table VII). Figure 4 gives a display of suggestive time history of ψ_{max} for $Gr = 28500$ (R–R–C). First, the computation (with 30 × 24) starting from the steady condition at $Gr = 28000$ converges towards a steady solution (part (a) of Figure 4): as given in Table VII, the spectral residual is nearly 8×10^{-3} at $t = 3$. Then, starting from this steady solution the computation is pursued with 40 × 30 and the periodic

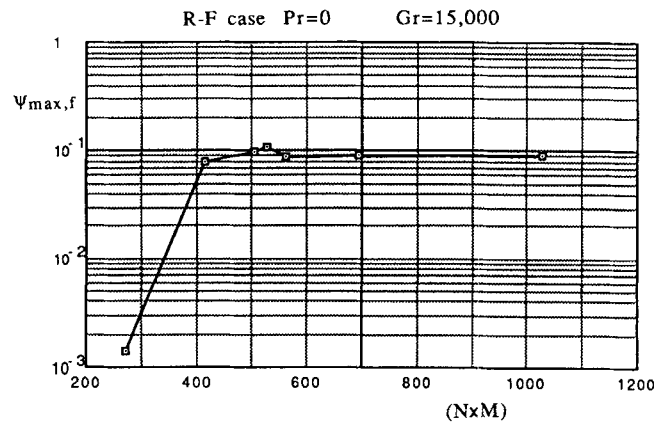

Figure 3. Effect of the resolution on the oscillation rate $\psi_{max,f}$ of the computed solution for $Gr = 15000$ in the R–F case for $Pr = 0$ (Table II).

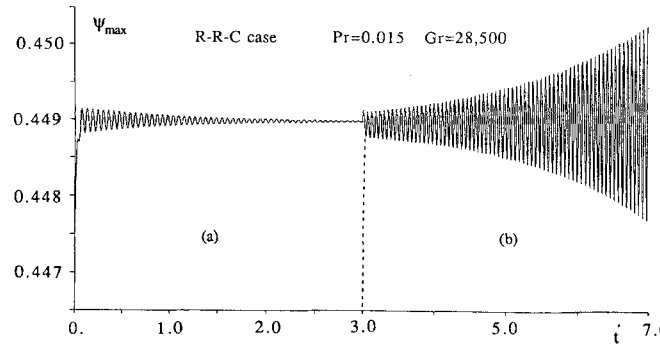

Figure 4. Effect of the resolution on the solution behaviour at $Gr = 28\,500$ in the R–R–C case (Table VII): (a) convergence towards a steady solution with 30 × 24 resolution for $0 \leqslant t \leqslant 3$; (b) convergence towards a time-periodic solution with 40 × 30 resolution for $3 \leqslant t \leqslant 7$. Note that the time abscissae used in parts (a) and (b) are different

solution is obtained at $t = 13{\cdot}5$. Part (b) of Figure 4 shows the beginning of the revival of the oscillations. A similar behaviour is observed for $Gr = 19\,000$ (R–F–A; see Table IV).

5. ANALYSIS OF THE FLOW REGIMES

The analysis is concerned with two cases according to the value of the Prandtl number. The case $Pr = 0$ is widely developed for the exploration of the effect of the Grashof number and the identification of the basic flow regimes. In that case the temperature equation is disregarded and the governing equations are (2) and (3) only where the temperature gradient is constant ($\partial\theta/\partial x = 1$). Then, computations using the full system (1)–(3) are done in the case $Pr = 0{\cdot}015$ with the main purpose of studying the thermal boundary effects. A number of basic flow patterns were determined by the simulation in the range of Gr and Pr, depending (sometimes) on the initial conditions. A number of flow regimes were identified and we have listed and characterized them briefly:

(i) *in the R–F case*

(a) a non-symmetric steady solution with one cell (one maximum value of ψ) denoted S1 (see Figure 5(a)(1))
(b) a non-symmetric steady solution with one primary cell and one secondary cell (two maximum values of ψ) denoted S11 (see Figure 5(a)(3))
(c) a time-periodic solution denoted P1 with a basic spatial structure analogous to S11 (see Figure 10)

(ii) *in the R–R case*

(a) a centrosymmetric steady solution with one cell (one maximum value of ψ) denoted S1
(b) a centrosymmetric steady solution with one primary cell and two secondary cells (three maximum values of ψ) denoted S12 (see Figure 11(a))
(c) a centrosymmetric steady solution with two co-rotating cells (ψ has two equal maxima) denoted S2 (see Figure 11(b))
(d) a time-periodic solution (fundamental frequency f) with the same centrosymmetric spatial structure as S12, denoted P1
(e) a quasi-periodic solution (two frequencies f and f_1) with a spatial structure analogous to P1

but without symmetry, denoted QP; sometimes one or two of the three maxima of ψ disappears (see Figure 16)

(f) a time-periodic solution (frequency $f/2$) denoted P2, with the same spatial structure as QP but with the flow pattern changing alternately between two- and three-cell structures corresponding to $\psi_{max,\,max}$ and $\psi_{max,\,min}$ respectively (see Figure 17).

5.1. Flow regimes for Pr = 0 and rigid–free conditions

5.1.1. Steady S1 and S11 regimes. The basic flow at low Gr is a one-cell circulation (Hadley circulation type) limited by the lateral confinement. A single vortex fills the entire cavity and is centred slightly above the midpoint (S1 solution). In Figure 5 the streamlines are given together with the vorticity and horizontal velocity patterns for $Gr = 117$. On increasing Gr, the vortex is stretched horizontally and its core is shifted downstream towards the cold wall (see Figure 5 for $Gr = 3124$) until it reaches a stable location at nearly mid-distance between the bottom and top walls and at less than one height from the cold wall (see Figure 5 for $Gr = 10\,000$). Stability analysis of the Hadley circulation cell for an infinite cavity and $Pr = 0$ predicts the onset of two-dimensional oscillatory motion at $Gr = 7580$ with $\lambda_x = 4{\cdot}6$.[19] The presence of the side walls with an extent ($A = 4$) smaller than the size of the predicted disturbance delays the threshold of oscillatory motion to higher Gr. Moreover, the confinement brings a significant change to the basic cellular flow. At $Gr = 10\,000$ a secondary vortex appears inside the basic cell structure (S11 solution): it arises in the hot region co-rotatingly with the primary vortex (a saddle point occurs between their cores). A similar flow pattern was depicted experimentally in a quite different shear-layer-driven cavity.[48] In this flow (as observed in our computed solutions) the onset of the secondary vortex is probably the result of the strong shear in the flow upstream of the primary vortex.

In Figure 6 we have plotted the variation of $Gr^{1/2}\psi_{max}$ in terms of Gr up to $Gr = 30\,000$ (above the onset of oscillation regimes). The steady solutions were mainly computed with a rather coarse (20×12) resolution, which explains the small irregularities shown in the vorticity pattern for $Gr = 12\,750$ (Figure 5). Nevertheless, the vorticity patterns emphasize the modification of the

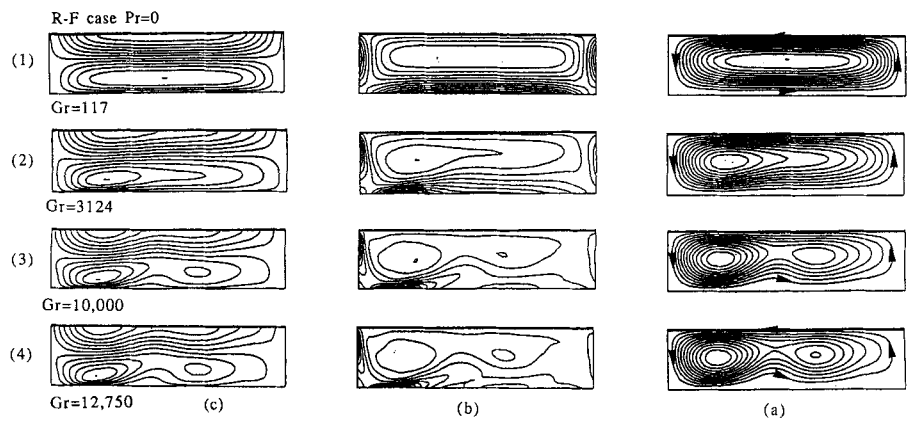

Figure 5. Steady regimes S1 and S11 in the R–F case for $Pr = 0$ (Table II): (a) streamlines, (b) iso-vorticity, (c) iso-horizontal-velocity component contour lines for (1) $Gr = 117$ ($\psi_{max} = 0{\cdot}058$, $\omega_{max} = 1{\cdot}34$), (2) $Gr = 3124$ ($\psi_{max} = 0{\cdot}318$, $\omega_{max} = 10{\cdot}94$), (3) $Gr = 10\,000$ ($\psi_{max} = 0{\cdot}547$, $\omega_{max} = 27{\cdot}18$), (4) $Gr = 12\,750$ ($\psi_{max} = 0{\cdot}593$, $\omega_{max} = 31{\cdot}73$). The iso-values corresponding to contourlines are separated by equal intervals of one-twelfth the maximal difference between extremal values of the variables

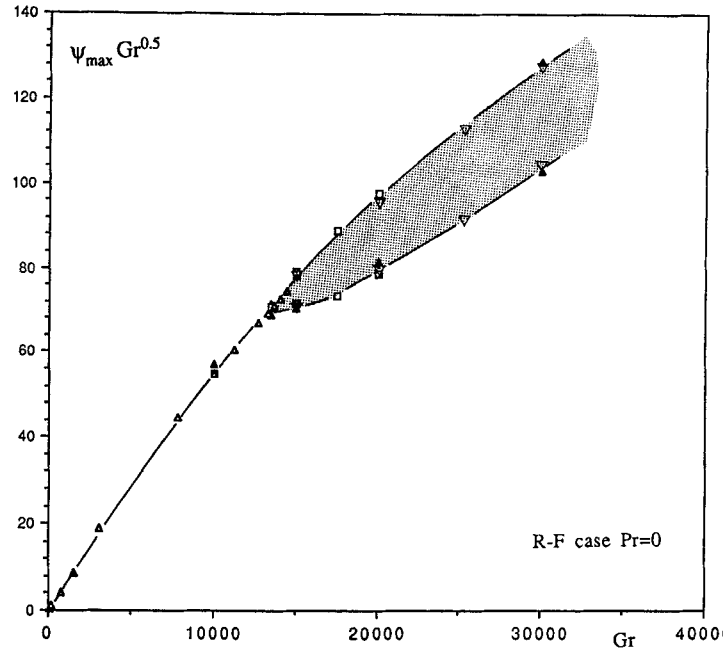

Figure 6. Identification of steady and time-dependent regimes in the R–F case for $Pr = 0$ (Table II). Variation of $\psi_{max} Gr^{1/2}$ versus Gr with resolutions of: Δ, 20 × 12; □, 27 × 15; ▲, 30 × 16; ▽, 32 × 16

shear stress at the cold and bottom rigid walls (in particular the two shear layers and the separation). The contourlines of the horizontal velocity component reflect similar features: the flow becomes more rapid near the cold wall when $Gr > 3000$. The maximum streamfunction (which is representative of the flow rate inside the fluid layer) is shown to follow nearly a linear Gr-dependence in the range of the steady regime.

5.1.2. Oscillatory P1 regime. The onset of time-dependent motion (P1 solution) is detected on the oscillation of ψ_{max} (the extremum values $\psi_{max,\,max}$ and $\psi_{max,\,min}$ are represented in Figure 6). Oscillations have been observed at $Gr \geqslant 13\,500$. This value is just below the critical Gr predicted by Winters[20, 28] (Table I).

For $Gr = 13\,500$, close to $Gr_{c,\,osc}$, the oscillation rate $\psi_{max,\,f}$ is rather sensitive to the resolution (Table II): it is about 3·9% for 30 × 16 and 30 × 24, 3·25% for 32 × 16 and 1·9% for 27 × 15. The transient stage to obtain stable oscillations is noticeably shortened when the initial condition is far enough from the solution (Figure 7). Then, for example, the oscillatory solution with 30 × 24 is not yet established at $t = 4$ when the steady solution at $Gr = 13\,000$ is taken as the initial condition (Figure 7(d)), and $\psi_{max,\,f}$ with 27 × 15 is only 0·54% at $t = 2{\cdot}9$ with the initial condition taken at $Gr = 13\,100$ (Figure 7(b)). The transient is obviously shorter ($t = 1$–2) when starting either from (11) (Figure 7(c)), from rest (Figure 7(b)) or from the time-dependent solution at $Gr = 15\,000$ (Figure 7(a)).

The transient to stable oscillation behaviour is even much shorter far from $Gr_{c,\,osc}$. As shown in Figure 8(a), the transient stage lasts nearly $t = 2$ for $Gr = 15\,000$ when starting from $Gr = 14\,500$. It is reduced to about $t = 0{\cdot}5$ for $Gr = 17\,500$ when starting from $Gr = 15\,000$, and to only $t = 0{\cdot}15$ for $Gr = 20\,000$ when starting from $Gr = 17\,500$. When the initial condition (11) is used at $Gr = 15\,000$, the oscillatory solution is established after less than $t = 1$ (Figure 8(b)). The

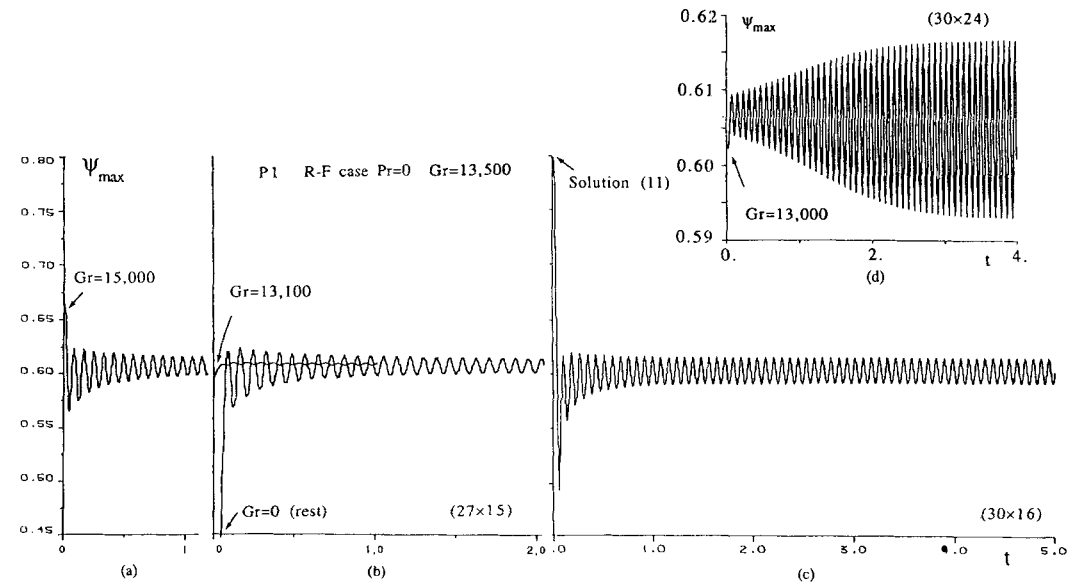

Figure 7. Onset of time-dependent regimes in the R–F case for $Pr = 0$ (Table II). Influence of initial conditions on the solution at $Gr = 13\,500$. Initial conditions from: (a) $Gr = 15\,000$ (oscillatory); (b) $Gr = 13\,100$ (steady) and $Gr = 0$ (rest); (c) equation (11); (d) $Gr = 13\,000$ (steady). Resolution: 27 × 15 for (a) and (b), 30 × 16 for (c) and 30 × 24 for (d)

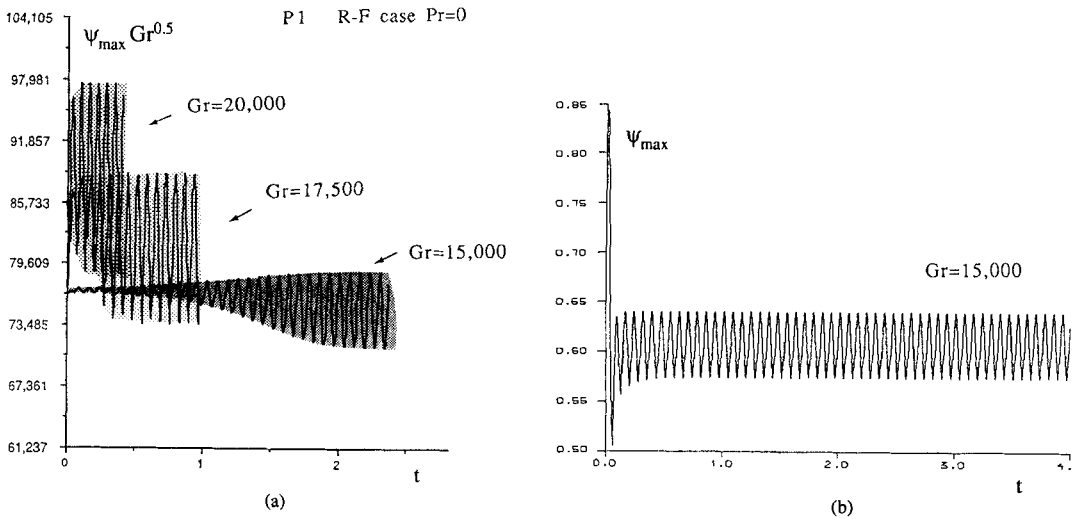

Figure 8. Time-periodic regime P1 in the R–F case for $Pr = 0$ (Table II). Variation of the initial transient stage of ψ_{max} versus time: (a) for $Gr = 15\,000$, 17 500 and 20 000 by successively incrementing Gr; (b) effect of initial condition (11) for $Gr = 15\,000$

oscillation rate $\psi_{max,f}$ versus Gr is shown in Figure 9(a). The threshold can be estimated by extrapolating the amplitude to zero and by assuming the behaviour $\psi_{max,f} \sim (Gr - Gr_{c,osc})^{1/2}$ as found in theoretical studies concerning the Hopf bifurcation. Considering the computed $\psi_{max,f}$ for $Gr = 13\,500$ and 15 000, the critical $Gr_{c,osc}$ is evaluated as 13 275 with an error ± 5 according to the spatial resolution considered. Then, by using $Gr_{c,osc} = 13\,270$, we represent

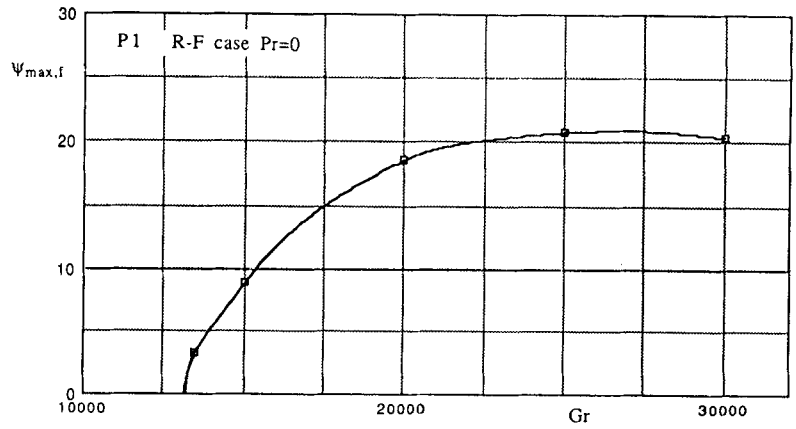

(a)

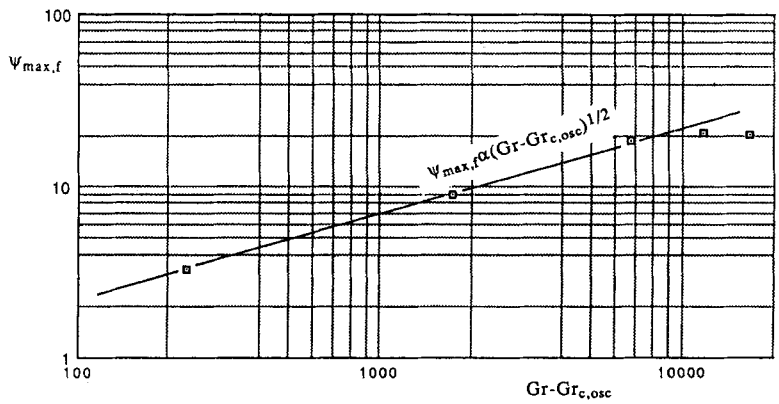

(b)

Figure 9. Time-periodic regime P1 in the R–F case for $Pr = 0$ (Table II): (a) variation of the amplitude of the oscillations $\psi_{max,f}$ (%) versus Gr; (b) $\psi_{max,f}$ (%) versus $Gr\text{-}Gr_{c,osc}$ with $Gr_{c,osc} = 13270$

$\psi_{max,f} \sim (Gr - Gr_{c,osc})^{1/2}$ and observe that the computed results fit fairly well up to $Gr = 20000$ (Figure 9(b)).

Figure 10 shows the time history of ψ_{max} for $Gr = 20000$ together with the instantaneous streamlines and countour lines for the vorticity at 10 distinct times equally spaced by an interval of 0·016 during a period. Note that the maximal values of ψ_{max} are taken on the grid of collocation points corresponding to a Chebyshev decomposition; the irregularities near the maximum of ψ_{max} result from this extremum travelling from one collocation point to a neighbour. The periodic motion is associated with the breathing of two vortices: the primary vortex grows and decays, the secondary grows then disappears, swallowed by the primary one. Separated (counter-rotating) flows develop at certain times of the period between the primary and secondary vortices, and between the secondary vortex and the hot wall (weaker separation). At $Gr = 13500$ we had already observed similar oscillations between one- and two-vortex patterns at the beginning of the adjustment stage, but this is rapidly damped and the resulting flow exhibits only a weakly pulsating two-vortex pattern. The one-to-two-vortex periodic solution already exists at

$Gr = 15\,000$.[27] At $Gr = 30\,000$ a movie film was made which emphasizes a more complex pattern: the separation flow below the two-vortex pattern becomes stronger and gives a vortex-shedding phenomenon with a counter-rotating vortex which arises and cuts the basic flow at the location of the saddle point.[49] Near the hot wall a separation region tends to appear while the secondary vortex is regressing and being swallowed by the primary one. The contourlines of the horizontal velocity complete the description of the flow and the vorticity contourlines emphasize the evolution of the shear stress, which varies in time mainly along the bottom wall.

Concerning the flow regimes at higher values ($Gr > 30\,000$), a number of complementary simulations were carried out in the range of Gr up to 220 000 using resolutions up to 64×32.[50] The main preliminary results have shown that (i) the P1 regime persists up to $Gr \approx 210\,000$, (ii) a chaotic behaviour is found at $Gr = 220\,000$ and (iii) the transition occurs via either a period-two or a period-three solution.

5.2. Flow regimes for Pr = 0 and rigid–rigid conditions

Because of the no-slip boundary conditions on all the walls, the critical Gr for the oscillatory R–R mode is higher than for the R–F case[17] and the solution tends to conserve the symmetry induced by the boundary conditions: the S1 and S12 steady solutions and the P1 time-periodic solution are centrosymmetric. At Gr close to 30 000 the symmetry is lost and the time-dependent solution is first governed by two frequencies (quasi-periodic QP solution) then by a second periodic behaviour different from P1 (P2 solution): the solution oscillates between a two-cell (S2) and three-cell (S12) structure. This competition between different modes of convection suggests the occurrence of a pairing behaviour as encountered in many situations where there is a breaking of (odd or even) symmetry. This precedes the change into a different spatial mode. In our case further increase of Gr brings a bifurcation of the solution to a steady mode of convection (S2) which involves two distinct cells in the horizontal direction. This kind of solution is found to be stable up to $Gr = 50\,000$ at least and to persist on decreasing Gr down to $Gr = 24\,500$, for which a (S12) solution still exists.

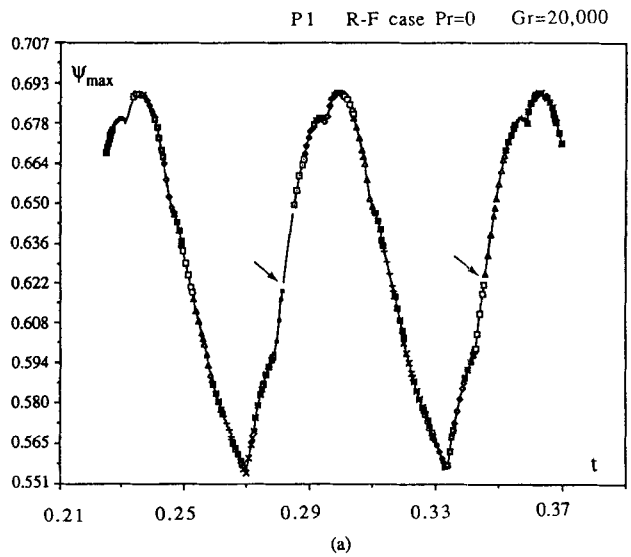

(a)

Figure 10. (a)

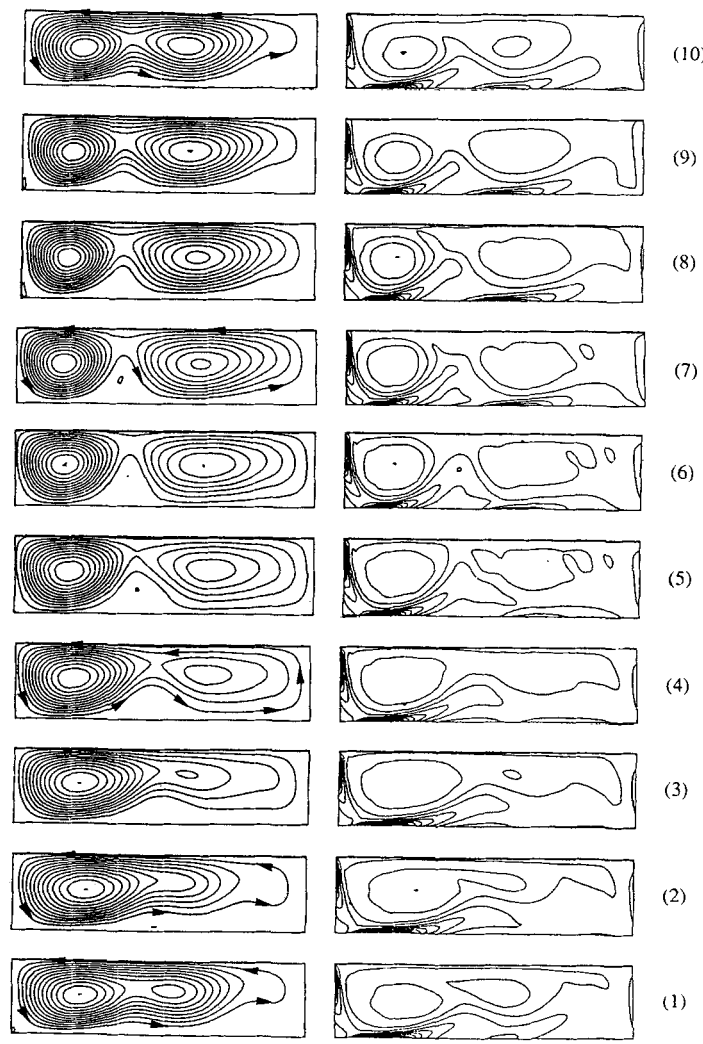

(b)

Figure 10. Time-periodic regime P1 at $Gr = 20\,000$ in the R–F case for $Pr = 0$ (Table II): (a) time history of ψ_{max}; (b) flow patterns at 10 time steps during a period of time. Instantaneous streamlines, iso-vorticity and iso-horizontal velocity component contourlines. The contourlines are separated by equal intervals of one-twelfth the difference between extremal values of the variables at each time step. The time steps start at $t \approx 0{\cdot}28$ and are separated by a 0·0064 interval. The maximal values of the variables (ψ_{max}, ω_{max}) are given at each time (n) as: (1) (0·642, 150·2); (2) (0·677, 157·6); (3) (0·687, 167·7); (4) (0·682, 162·9); (5) (0·648, 146·4); (6) (0·619, 143·9); (7) (0·588, 127·6); (8) (0·567, 123·6); (9) (0·568, 125·1); (10) (0·589, 142·5)

The details of these solutions are given in Table III and in the following sub-sections. The calculations were carried out in the range $10\,000 \leqslant Gr \leqslant 50\,000$ with method I except in one case, for $Gr = 30\,000$, where method II was also used in order to confirm the occurrence of a quasi-periodic behaviour. Note that at a given Gr we always obtained the same solution when starting from the asymptotic solution (11) or a centrosymmetric solution (S1 or S12) as the initial condition: S1 then S12 for $Gr \leqslant 25\,500$; P1 for $26\,000 \leqslant Gr \leqslant 28\,500$; QP for

$29\,500 \geqslant Gr \leqslant 30\,450$; P2 for $30\,500 \leqslant Gr \leqslant 33\,000$; S2 for $Gr \geqslant 33\,500$. On the other hand, a second solution S2 can also be obtained in the range $24\,000 < Gr < 33\,500$ when starting from an S2 initial condition. In the following sub-sections the discussion will be organized in three parts. First we consider the steady solutions obtained with the asymptotic solution (11) as the initial guess or when Gr is increased by progressive steps below the threshold of the Hopf bifurcation (steady S1 and S12 regimes). In the second part we analyse carefully the onset of the oscillatory motion, the transition to a quasi-periodic behaviour with frequencies f, f_1 and the second transition to a periodic behaviour with frequency $f/2$. The third section is devoted to the steady (S2) regime and to the hysteresis effect observed when decreasing Gr down to 24 500.

5.2.1. Steady S1 and S12 regimes. Starting the computation with the initial condition (11) for $Gr = 10\,000$, the solution converges to an S1 solution. For larger Gr up to 25 500 an S12 solution is obtained (Table III). Figure 11(a) displays the steady flow pattern and the convergence history for $Gr = 25\,000$. The flow at $Gr = 10\,000$ is slightly different from the basic monocellular Hadley circulation. It is no longer strictly parallel in the core region and the turning of the flow by the end walls extends to the centre section of the cavity. However, a fully established instability still cannot be identified at this Gr value. At $Gr = 25\,000$ the size of the major cell is nearly 1·6. The instability predicted by theory at $Gr > 7942$ is steady[17, 19] and the critical wave number ($\lambda_x = 2{\cdot}34$) is smaller than the aspect ratio of the cavity. The steady solutions suggest that the onset of a steady instability should occur at $Gr > 10\,000$ and that the corresponding wave number should reduce on increasing Gr. Then the linear stability analysis seems to be possibly somewhat realistic for a finite cavity at $A = 4$ even if it is not able to predict the second transition to a time-dependent behaviour.

5.2.2. Time-dependent P1, QP and P2 regimes. For the study of time-dependent regimes we were careful to perform the computations over a long period of time during which the solution behaviour remains unchanged. Nevertheless, we do not claim that the solutions maintain the same behaviour if the computation is pursued further.

The solution becomes time-dependent (P1) on increasing Gr to 26 000. The spatial structure of the flow remains similar to S12 observed for $Gr = 25\,500$. Oscillatory flows are obtained for Gr up to 33 000 (Table III) but they are no longer P1 when $Gr \geqslant 29\,500$. From the calculations effectively performed, the critical Grashof number $Gr_{c,\,osc}$ at the onset of oscillations lies between

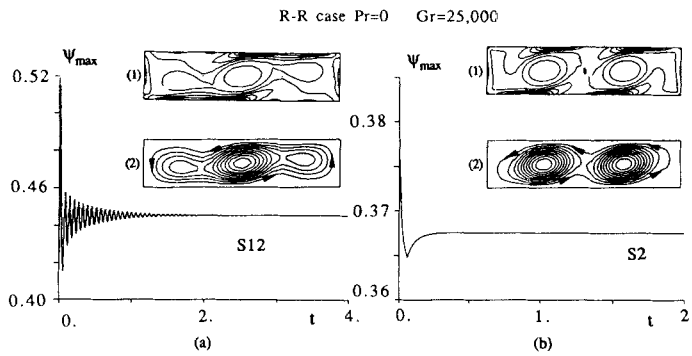

Figure 11. Steady regimes S12 and S2 in the R–R case for $Pr = 0$ (Table III). Time history of ψ_{max} and steady flow patterns ((1) vorticity and (2) streamlines) for $Gr = 25\,000$. Occurrence of two possible steady solutions depending on initial conditions: (a) asymptotic S1-type solution (11), refer to run $25\,000^{(b)}$ in Table III; (b) S2-type steady solution at $Gr = 26\,000$, refer to run $25\,000^{(d)}$ in Table III

25 500 and 26 000. This result agrees quite well with the value $Gr_{c,osc} = 25\,525$ calculated by Winters.[20] The oscillatory solutions are characterized by the fundamental frequencies f reported in Table III.

When starting from the P1 solution at $Gr = 28\,500$, the time history of ψ_{max} at $Gr = 29\,500$ first exhibits a P1 behaviour (with one frequency f) over a long time $t \approx 8$, then self-sustained disturbances arise and settle down quickly into a QP behaviour. During the transient state the symmetry of the flow is lost and a second frequency f' (which is incommensurate with f) appears corresponding to the modulation of ψ_{max}. The QP solutions are obtained in the range $29\,500 \leqslant Gr \leqslant 30\,450$ and the frequency f' is observed to diminish as Gr increases (see Figures 12–14). Note that the establishment of the QP regime is obtained at $t \approx 2{\cdot}5$ for $Gr = 30\,000$ when starting from $Gr = 25\,500$ and at $t \approx 8$ for $Gr = 29\,500$ when starting from $Gr = 28\,500$. More precisely we obtained successively: $f = 17{\cdot}45 \approx 6f'$ for $Gr = 29\,500$; $f = 17{\cdot}55 \approx 9f'$ for $Gr = 30\,000$; $f = 17{\cdot}56 \approx 10f'$ for $Gr = 30\,100$; $f = 17{\cdot}52 \approx 15f'$ for $Gr = 30\,300$; $f = 17{\cdot}53 \approx 22f'$ for $Gr = 30\,400$; $f = 17{\cdot}50 \approx 36f'$ for $Gr = 30\,450$. The time histories of ψ_{mid} and ψ_{quart} are given for some of these Grashof numbers in Figures 13(a)–13(d) and 14(a)–14(d) respectively. The time histories reveal the modification of the frequency f' with Gr. Figures 13(e) and 14(e) show that the regime is no longer quasi-periodic at $Gr = 30\,500$.

The above results have been obtained with 40 × 30. In order to determine the possible effect of the spatial resolution, the solution at $Gr = 30\,000$ was computed with different resolutions (see Table III). With the low (30 × 16) resolution we obtain $f = 17{\cdot}43 \approx 7f'$, which reveals a rather important change in the frequency of modulation. The results do not significantly change with respect to the case 40 × 30 on increasing the resolution up to 100 × 80 during the QP regime. Figure 15 shows the time histories of ψ_{mid} obtained during a modulation for four different resolutions, together with the variation of the extrema of ψ_{mid} plotted with respect to the number of Chebyshev polynomials (Figure 15(e)). With 40 × 30 the QP behaviour is established after a transient time longer than that with 30 × 16. The transient time can be significantly shortened by introducing disturbances during the P1 stage. (The disturbances correspond to a 50% increase of $\psi(A/4, 1/4)$.) This suggests that the P1 solution is weakly unstable. On the other hand, the stability of the QP regime is confirmed with respect to 100% disturbances superimposed on the solution.

Figure 16 exhibits the streamlines for $Gr = 30\,000$ at 10 instants during the modulation. By observing these pictures we notice a break of symmetry, the solution oscillating between two- and three-cell states. Furthermore, the central cell is always the most important, with a magnitude often twice as large as the secondary cells. Note that we observe at some instants a pairing behaviour when one of the secondary cells is swallowed by the major one. Also, regions of weak

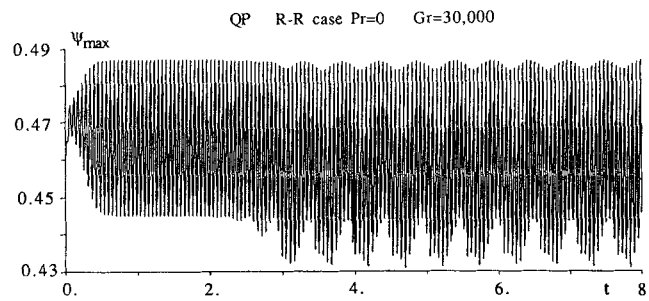

Figure 12. Time-dependent QP regime in the R–R case for $Pr = 0$ (Table III). Time history of ψ_{max} at $Gr = 30\,000$ with 40 × 30 resolution, refer to run $30\,000^{(d)}$ in Table III. Initial condition from steady S12 solution at $Gr = 25\,500$

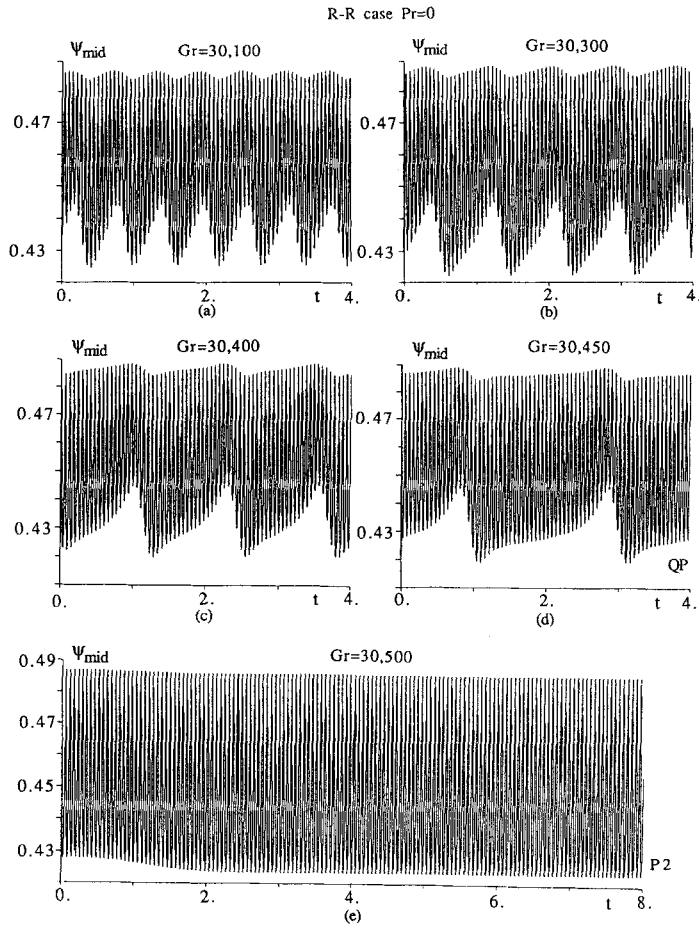

Figure 13. Time-dependent QP and P2 regimes in the R–R case for $Pr = 0$ (Table III). Time histories of ψ_{mid} at (a) $Gr = 30\,100$, (b) 30 300, (c) 30 400, (d) 30 450, (e) 30 500 with 40 × 30 resolution. QP-type solution for (a)–(d) and P2-type solution for (e)

separation flow appear near the horizontal walls in the neighbourhood of the saddle points (the dotted lines correspond to $\psi = 0$).

At $Gr = 30\,500$ the solution is no longer QP periodic. The streamlines are given in Figure 17 for $Gr = 31\,000$ at eight instants during two consecutive oscillations, together with the time history of ψ_{max}. The latter shows a periodicity with frequency $f = 17{\cdot}12$ (Figure 17(b)) while the flow patterns in Figure 17(a) show a periodicity with frequency $f/2 = 8{\cdot}56$ (see the skew symmetry, for instance, in the streamline patterns (1), (5) and (3), (7) at two consecutive times separated by $1/f$). This shows that the maximum of ψ is always close to the midpoint of the domain and is practically unaffected by the $f/2$ behaviour. Similarly, the time history of ψ_{mid} for $Gr = 30\,500$ (Figure 13(e)) exhibits the same behaviour as described above for ψ_{max}. On the other hand, the history of ψ_{quart} (Figure 14(e)) clearly shows the actual periodicity of the flow characterized by the frequency $f/2$. In the range $30\,500 \leqslant Gr \leqslant 33\,000$ the solution is P2. A power spectrum analysis was performed on ψ_{mid} and ψ_{quart} for $Gr = 30\,500$ (Figure 18(a)). This confirms

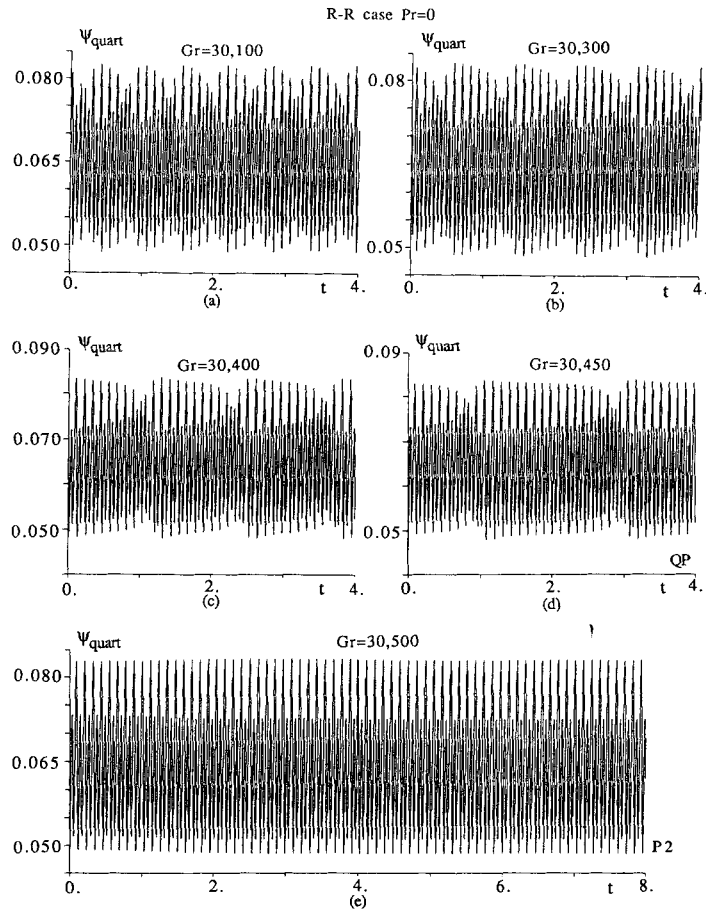

Figure 14. Time-dependent QP and P2 regimes in the R–R case for $Pr = 0$ (Table III). Time histories of ψ_{quart} at (a) $Gr = 30100$, (b) 30300 (c) 30400, (d) 30450 (e) 30500 with 40 × 30 resolution. QP-type solution for (a)–(d) and P2-type solution for (e)

that the $f/2$ frequency, although present in the ψ_{mid} history, has a negligible amplitude. On the other hand, it is almost half the amplitude of the fundamental for ψ_{quart}.

Coming back to the QP regime, the power spectra of ψ_{mid} and ψ_{quart} for $Gr = 30000$ (Figure 18(b)) reveal the following features. The power spectrum of ψ_{mid} exhibits a second frequency f' with an amplitude only one order of magnitude smaller than that of the fundamental. The power spectrum of ψ_{quart} also exhibits this f' frequency but with an amplitude three orders of magnitude smaller than that of the fundamental. Moreover, it reveals the presence of two frequencies f_1 and f_2 which are only one order of magnitude below the fundamental. The frequencies are $f_1 = 9{\cdot}809$ and $f_2 = 7{\cdot}797$ with $f = 17{\cdot}605$ and $f' = 2{\cdot}012$. The following relations exist between f, f', f_1 and f_2: $f' = -f + 2f_1 = f - 2f_2$; thus $f_1 - f_2 = f'$ and $f_1 + f_2 = f$, suggesting that the QP behaviour is better characterized by the frequencies f and f_1 and that f' and f_2 are linear combinations of these. We note that f_1 and f_2 are symmetrically close to $f/2$, which suggests the occurrence of a strong resonance phenomenon.[51] Then, as Gr is increased, f_1 tends towards $f/2$ while $f_2 \to f/2$ and $f' \to 0$, as revealed by the analysis of Figure 14. The periodic regime

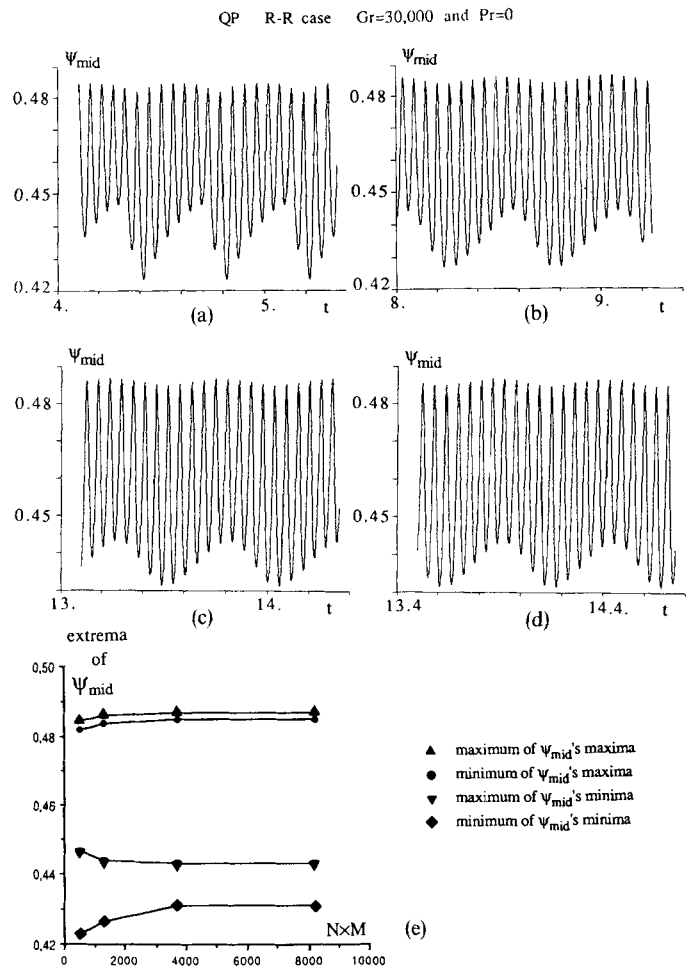

Figure 15. Effect of the resolution on QP time-dependent solution at $Gr = 30\,000$ in the R–R case for $Pr = 0$ (Table III). Time-histories of ψ_{mid} with (a) 30 × 16, (b) 40 × 30, (c) 60 × 60 and (d) 100 × 80 resolutions. (e) Variation of the extrema of ψ_{mid} with resolution

obtained is in fact characterized by the subharmonic solution of frequency $f/2$, originated from a strong resonance phenomenon.

5.2.3. Reverse transition to steady S2 regime. At $Gr = 33\,500$ we obtain a steady solution S2, and the ultimate two-cell flow pattern is shown in Figure 19. This centrosymmetric solution presents a strong periodic feature in the horizontal direction. In comparison with Figure 11(b) obtained for a smaller Gr, the coupling between the two cells is weakening as their sizes decrease with increasing Gr. Independently of initial conditions we always obtain the same S2 solution in the investigated range of Gr ($33\,500 \leqslant Gr \leqslant 50\,000$). This steady state is obtained more or less rapidly as discussed in Section 4.2 for $Gr = 50\,000$. Note that a two-cell initial condition reduces substantially the duration of the transient stage. As a result one could surmise that the three-cell solution observed in the transient stage is in fact weakly unstable.

Starting from the solution computed at $Gr = 35\,000$, the S2 solution persists down to $Gr = 24\,500$. The values of $\psi_{max,\,max}$ are reported in Figure 20, which summarizes the results

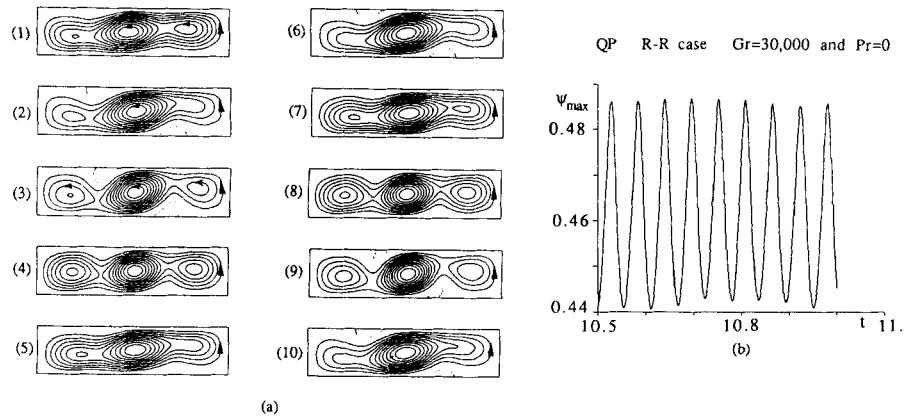

Figure 16. Time-dependent QP (40 × 30) solution at $Gr = 30000$ in the R–R case for $Pr = 0$ (Table III): (a) streamline patterns at 10 time steps during a double period; (b) time history of ψ_{max}. Time steps at (1) $t = 10{\cdot}5150$, (2) 10·5296 ($\psi_{max,\,max}$), (3) 10·5384, (4) 10·5546 ($\psi_{max,\,min}$) (5) 10·5747, (6) 10·5844 ($\psi_{max,\,max}$), (7) 10·5982, (8) 10·6108 ($\psi_{max,\,min}$), (9) 10·6290, (10) 10·6405 ($\psi_{max,\,max}$)

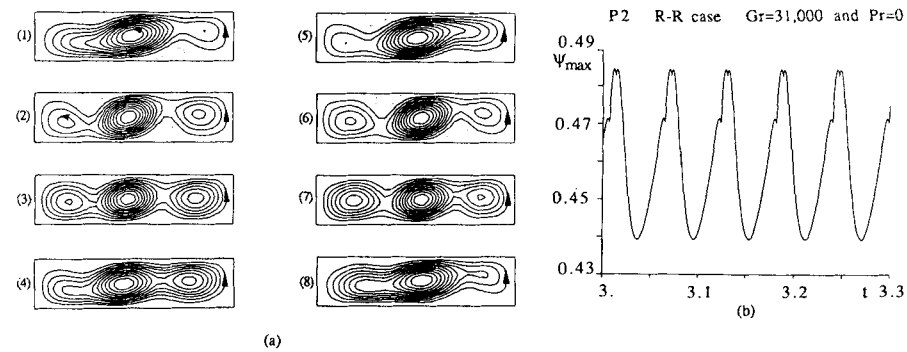

Figure 17. Time-dependent P2 solution at $Gr = 31000$ in the R–R case for $Pr = 0$ (Table III): (a) streamline patterns at eight time steps during a double period; (b) time history of ψ_{max}. Time steps at (1) $t = 3{\cdot}1287$ ($\psi_{max,\,max}$), (2) 3·1394, (3) 3·1540 ($\psi_{max,\,min}$), (4) 3·1719, (5) 3·1871 ($\psi_{max,\,max}$), (6) 3·1973, (7) 3·2125 ($\psi_{max,\,min}$), (8) 3·2389

discussed in this sub-section. The results obtained for $24500 \leqslant Gr \leqslant 33450$ prove the existence of a hysteresis effect: two different solutions can be obtained simultaneously in the range—on one side S2, on the other side either S12 or P1 or QP or P2. The dotted arrowed lines represent the transition existing between the two kinds of solutions. The transition P2 → S2 is determined accurately. The transition S2 → S12 between steady solutions suggests that the lower bound of the hysteresis cycle is located between $Gr = 24000$ and 24 500.

5.3. Effect of variable temperature field and thermal boundary conditions for Pr = 0·015

The influence of a variable temperature field was investigated for $Pr = 0{\cdot}015$. One of the purposes is to check if the results obtained for the $Pr = 0$ problem are realistic for low-Pr situations. Calculations were performed with method I and the results are given in Tables IV–VII.

We have observed that the same steady (S1 and S11) and time-periodic (P1) regimes exist in the R–F case for $Pr = 0{\cdot}015$ (conducting and insulating wall cases) as for $Pr = 0$ but at higher

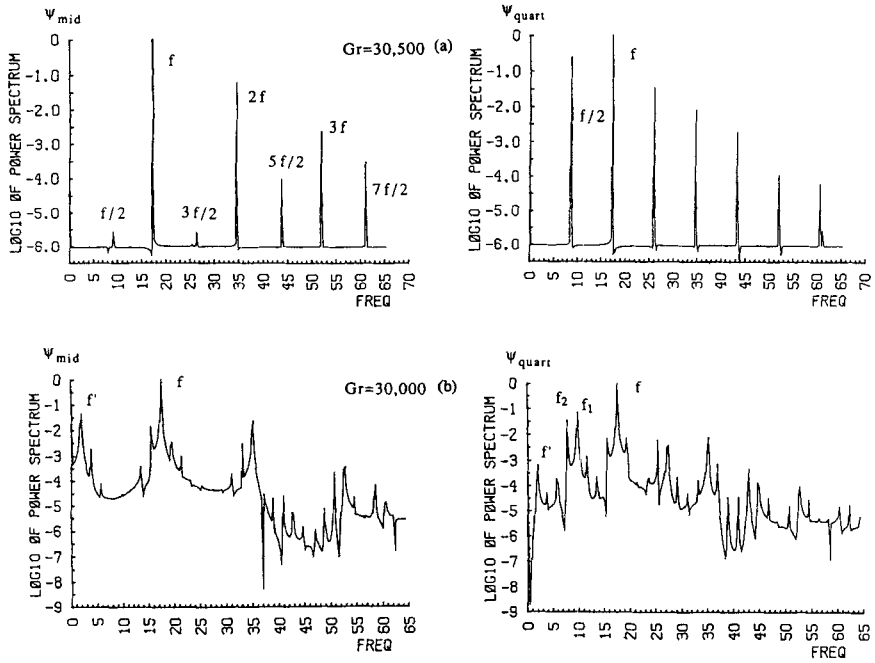

Figure 18. Time-dependent QP and P2 solutions in the R–R case for $Pr = 0$ (Table III): (a) power spectrum analyses of ψ_{mid} and ψ_{quart} for $Gr = 30\,500$; (b) for $Gr = 30\,000$

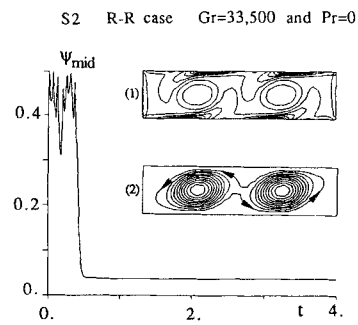

Figure 19. Steady state S2 solution at $Gr = 33\,500$ in the R–R case for $Pr = 0$ (Table III): time history of ψ_{mid} with (1) vorticity and (2) streamline patterns

thresholds. Such a behaviour is predicted by the theoretical analyses. We did not investigate the case $Pr = 0{\cdot}015$ as extensively as the case $Pr = 0$. For example, the hysteresis effect has not been investigated. However, the calculations performed with $Pr = 0{\cdot}015$ have exhibited similar behaviours; in the R–R–C case the solutions S12, P1, QP, P2 and S2 are identified. The R–R–A case corresponds to higher thresholds: the onset of the P1 regime is estimated close to $Gr = 33\,500$. In the range up to $Gr = 40\,000$ we only obtained the S12 and P1 regimes, while the QP and P2 regimes should arise at $Gr > 40\,000$.

Insulating horizontal wall conditions lead to a delay in the onset of oscillatory convection as noticed by Winters.[20] For the R–F–A case $Gr_{c,\,osc} \approx 19\,000$ (increase of about 29% compared to the R–F–C case) and for the R–R–A case $Gr_{c,\,osc} \approx 33\,500$ (increase of 17·5% compared to the

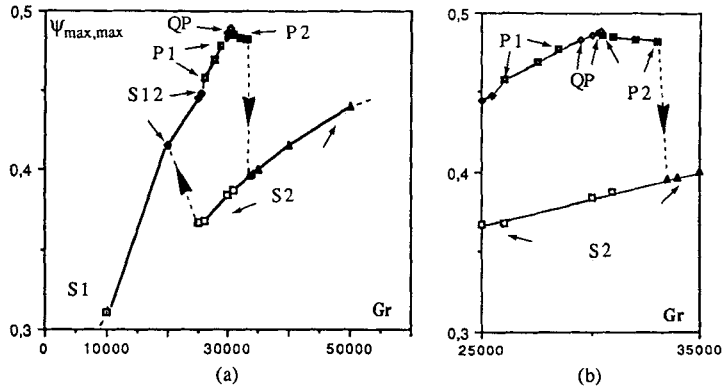

Figure 20. Identification of a hysteresis cycle in the R–R case for $Pr = 0$ (Table III): (a) $\psi_{max,\,max}$ versus Gr for $10\,000 \leqslant Gr \leqslant 50\,000$; (b) blow-up of range $25\,000 \leqslant Gr \leqslant 35\,000$

R–R–C case) (see Table I). The comparisons with Winters' results show that his values of $Gr_{c,\,osc}$ are 13·6% larger than ours in the R–R–A case and 12·6% smaller than ours in the R–F–A case. In this last case, however, our value of $Gr_{c,\,osc}$ is in fairly good agreement with the value (20 500 ± 250) recently obtained by Sani and Carpenter[52] using direct simulation through a finite difference method (30 × 90 to 40 × 120 graded meshes). Note that for the R–F–A and R–R–A cases our main aim was the determination of the thresholds. Here the computations were performed up to $Gr = 40\,000$, only; this range of Gr allows for comparisons with the S12 and P1 regimes for the R–R–A case and with the S12, P1, QP, P2 and S2 regimes for the R–R–C case. Figure 21 displays the vorticity, streamline and isotherm patterns for $Gr = 30\,000$ (R–F–A) at six instants during a period of the established oscillatory solution, starting at the time corresponding to the maximum of ψ_{max}. The distortions of the temperature fields appear to remain relatively limited during the cycle.

We now describe the main results obtained with the conducting wall conditions. For the R–F–C case $Gr_{c,\,osc} \approx 14\,700$ and for the R–R–C case $Gr_{c,\,osc} \approx 28\,500$. These values are in good agreement with those found by Winters (see Table I). In the R–F–C case the solutions computed for increasing values of Gr up to 20 000 show the same subsequent regimes as for $Pr = 0$ (see Table V).

Let us now give some details about the computations performed in the R–R–C case. The computed solution is P1 in the range $28\,500 \leqslant Gr \leqslant 35\,000$, QP for $35\,000 \leqslant Gr \leqslant 37\,000$, P2 up to $Gr = 40\,000$ and finally an S2 solution was found for $Gr = 45\,000$ (Table VII). For $Gr = 35\,000$ the solution is still P1 at $t = 8$ with 40 × 30 resolution and an initial condition of type P1, while we get a QP regime as soon as $t = 2$ with 30 × 16 resolution starting from initial condition (11). As in the $Pr = 0$ case we observe the modulation of $\psi_{max,\,f}$ corresponding to frequencies $f' = 3{\cdot}9$ for $Gr = 35\,000$, 3·3 for $Gr = 35\,500$, 2·6 for $Gr = 36\,000$, 1·8 for $Gr = 36\,500$ and 0·7 for $Gr = 37\,000$. Again we observe the frequencies f_1 and f_2 such that $f_1 + f_2 = f$ and $f_1 - f_2 = f'$. Figure 22 shows the time-history of the temperature θ_{mid} at the midpoint of the cavity during the QP regime for $Gr = 37\,000$. Figure 23 illustrates the P2 solution obtained for $Gr = 40\,000$ when starting from $Gr = 28\,500$. The solution is P1 during the first stage then settles down to a P2 solution. The transition between the two states is associated to the loss of flow symmetry and is emphasized by the time histories of ψ_{max} and θ_{mid} in Figures 23(a) and 23(b). During the non-symmetric phase P2, θ_{mid} oscillates between 2·035 and 1·965 (Figure 23(c)), while it remains constant at its mean value during the centrosymmetric stage P1. As for $Gr = 31\,000$ and $Pr = 0$, a complete time

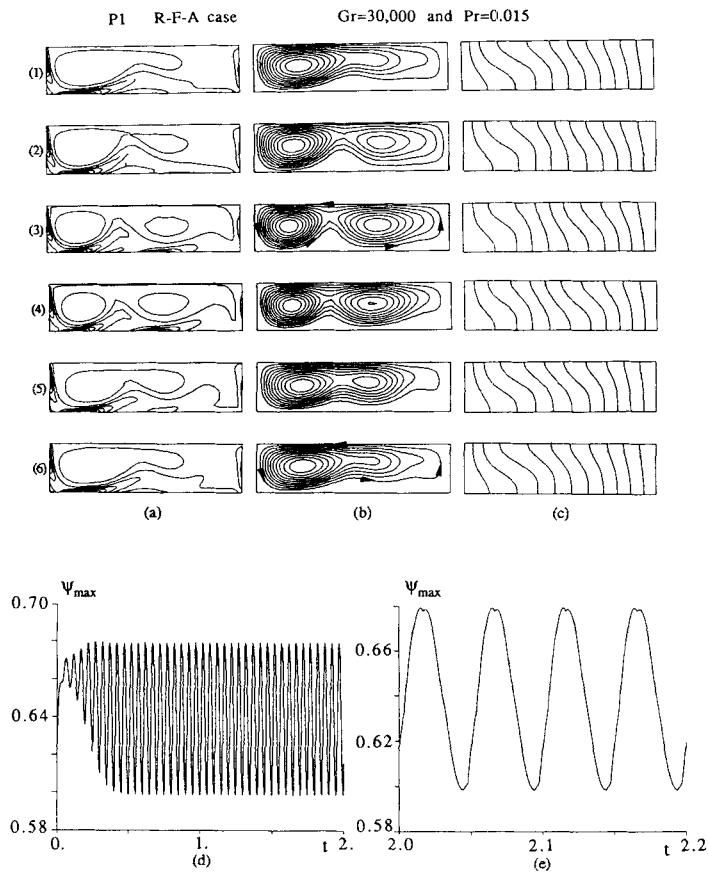

Figure 21. Time-periodic P1 regime in the R–F–A case for $Pr = 0{\cdot}015$ and $Gr = 30\,000$ (Table IV): (a) iso-vorticity, (b) streamline and (c) isotherm patterns at six time steps during a period of P1 solution; (d) time history of ψ_{max}; (e) enlargement of the last four periods of the asymptotic oscillatory state. Time steps at (1) $t = 2{\cdot}0149$ ($\psi_{max,\,max}$), (2) 2·0250, (3) 2·0350, (4) 2·0442 ($\psi_{max,\,min}$) (5) 2·0550, (6) 2·0625

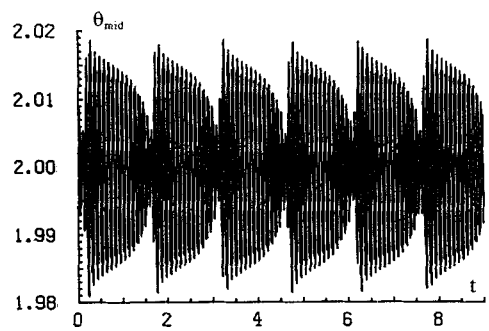

Figure 22. Time-periodic QP regime in the R–R–C case for $Pr = 0{\cdot}015$ and $Gr = 37\,000$ (Table VII): time history of θ_{mid} for $0 \leqslant t \leqslant 9$ with 30×16 resolution

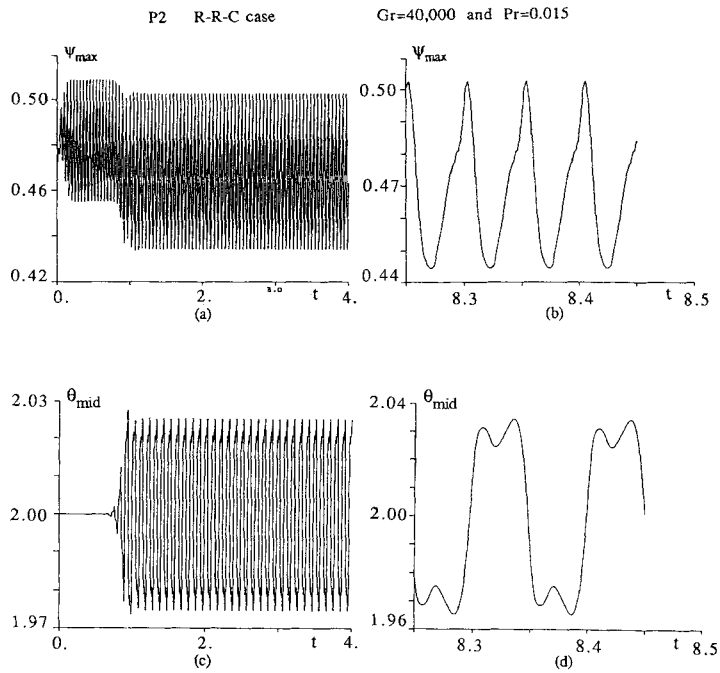

Figure 23. Time-periodic P2 regime in the R–R–C case for $Pr = 0{\cdot}015$ and $Gr = 40\,000$ (Table VII): time histories of (a) ψ_{max} and (c) θ_{mid} for $0 \leqslant t \leqslant 4$ with 30×24 resolution and of (b) ψ_{max} and (d) θ_{mid} for $8{\cdot}25 \leqslant t \leqslant 8{\cdot}45$ with 90×80 resolution

period of the flow corresponds to two cycles of ψ_{max} (Figure 23(d)). The time history of θ_{mid} is more clearly representative of the actual periodicity of the P2 regime. On checking the accuracy of the solution for $Gr = 40\,000$ (see Table VII), we do not observe any qualitative change when the resolution varies from 30×24 to 90×80 and only a slight difference in the amplitude of oscillation is noticeable when the resolution goes from 30×24 to 40×30. The slight discrepancy in $\psi_{max,\,f}$ shown in Table VII is attributed to a collocation effect: the maximum of ψ is computed on the grid of the collocation points, which changes when the resolution is modified.

Concerning the flow patterns shown by Winters[20] for these cases, we observe some obvious similarities with our direct simulations. In the R–F–C case the streamline patterns exhibit an oscillation between one- and two-cell configurations. However, a major difference is sought because the main cell is shown by Winters' expansion solution to move between the hot and cold sides of the cavity, the centre of the cell travelling similarly. In our computations the solution corresponds to the breathing of the two-cell structure: close to $Gr_{c,\,osc}$ the pattern remains of the two-cell type but with fluctuating cells. For Gr much larger than $Gr_{c,\,osc}$ the flow oscillates between one- and two-cell patterns, but the major cell always remains located near the cold side even if it expands into the hot region to swallow the secondary cell during the period. Also, the solution that we obtained in the R–R–C case near the threshold at $Gr = 30\,000$ oscillates between a main centred cell and two secondary side cells. These secondary cells are present during the entire period but never reach the same vertical height as the major one, as suggested by Winters' solutions. Figure 7 in Winters' paper[20] shows the visualization of the oscillatory flow arising near the Hopf bifurcation. It reveals the existence of a one-cell configuration during more than one-half of the cycle. The side cells arise temporarily and disappear. Such a behaviour (one-to-three-cell configuration) was not found in our computed solutions near the first bifurcation but at a

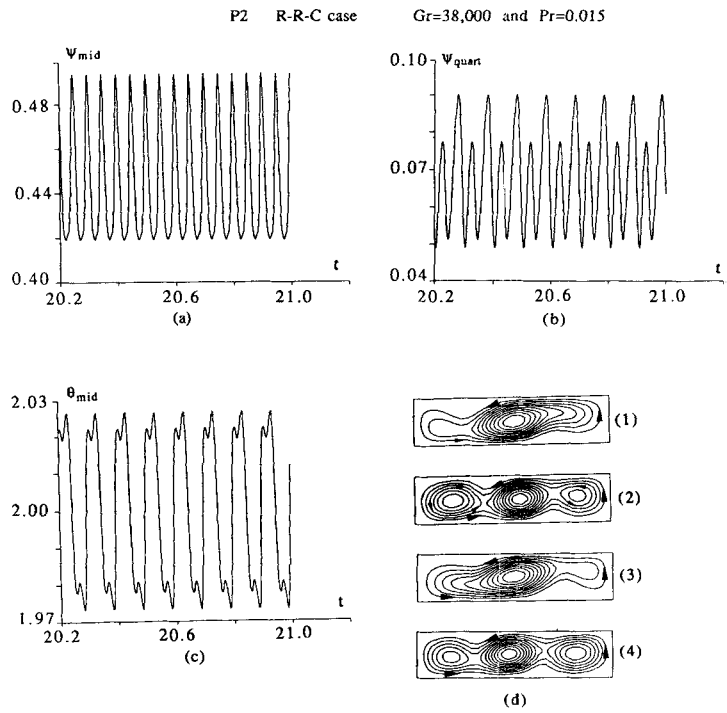

Figure 24. Time-periodic P2 regime in the R–R–C case for $Pr = 0{\cdot}015$ and $Gr = 38\,000$ (Table VII): time histories of (a) ψ_{mid}, (b) ψ_{quart} and (c) θ_{mid} with 40×30 resolution. (d) Streamline patterns at four time steps during a period of P2 solution. Time steps at (1) $t = 20{\cdot}7993$ ($\psi_{max,\,max}$), (2) $20{\cdot}8235$ ($\psi_{max,\,min}$), (3) $20{\cdot}8496$ ($\psi_{max,\,max}$), (4) $20{\cdot}8738$ ($\psi_{max,\,min}$)

certain distance from $Gr_{c,\,osc}$ after the transition to the P2-type solution characterized by the half-frequency $f/2$ (see Figure 24 for $Gr = 38\,000$).

6. CONCLUSIONS

Flows of a low-Prandtl-number fluid inside a differentially heated cavity have been calculated using tau-Chebyshev methods. The limiting case $Pr = 0$ and the case $Pr = 0{\cdot}015$ have been considered with a variety of boundary conditions for dynamical quantities (no-slip or stress-free walls) and temperature (conducting or insulating walls). For each configuration a finite set of Grashof numbers has been investigated. Also, a finite time of integration has been considered for unsteady calculations. It is obvious that these two facts must be kept in mind when conclusions are drawn, even if a large number of runs have been performed.

In the case $Pr = 0$ calculations have been conducted with two different methods and the results obtained by both are in perfect agreement. In the rigid–free configuration two types of solutions have been determined according to the value of the Grashof number: steady solutions for lower values and a time-periodic solution for larger ones. For the rigid–rigid case the threshold of the oscillatory motion is increased and the variety of solutions is larger: steady, periodic and quasi-periodic solutions. For large values of Gr the flow again becomes steady and remains so on decreasing Gr, exhibiting a hysteresis cycle.

When $Pr = 0{\cdot}015$ the threshold for each bifurcation is increased compared to that observed in the $Pr = 0$ case and, moreover, is higher in the insulating case than in the conducting case. Again,

in the investigated range of Grashof numbers, steady and periodic solutions have been exhibited as in the $Pr = 0$ case. This shows that $Pr = 0$ solutions give realistic predictions for the regimes in a range of low-Pr problems (at least up to $Pr = 0{\cdot}015$). The results obtained for $Pr \neq 0$ suggest that the oscillations of the flow do not originate from possible fluctuations occurring in the temperature field.

From the numerical point of view, method II (based on LSODA) is generally less time-consuming than method I when only steady regimes are of interest. Method II is also efficient for time-dependent solutions in the case of moderate resolution; however, for large resolutions method I is to be recommended. The influence matrix technique (method I) guarantees rather good stability conditions. The R–F conditions generate high speed levels which place more restriction on the time step than in the R–R case. Both solution methods are in very good agreement from the accuracy point of view. The threshold of the oscillations in the R–F case was found with only about 10% discrepancy when using a coarse resolution. (With classical methods the accurate determination of the threshold can require large resolution.) Moreover, using a limited spatial resolution we have identified elsewhere the various regimes encountered in the R–R case with only small differences in the thresholds.

The R–R case presents a larger variety of regimes than the R–F case, although the velocity scales are smaller. Multiple solutions were shown to exist over a range of Gr which give rise to a complex hysteresis cycle involving steady, periodic and quasi-periodic regimes. The methods have also been tested by the authors in the $Pr = 0$ case in order to investigate the transition to the chaotic regimes in the R–F case[50] and the occurrence of secondary hysteresis cycles in the R–R case.[53]

ACKNOWLEDGEMENTS

The computations were carried out on a Cray2 computer with support from CCVR. Research support from CNRS, MRES, DRET and CNES in France is gratefully acknowledged. E.C.A wishes to acknowledge support from Comunidad de Madrid, DGICYT and MEC in Spain. This work was carried out partly for the purpose of preparing the GAMM Workshop on Numerical Simulation of Oscillatory Convection in Low Pr Fluids organized by Dr. B. Roux in Marseille (October 1988). The authors also wish to thank J. M. Vanel for his contribution to the elaboration of Method I, Dr. A. C. Hindmarsh for use of the LSODA solver, and Professors P. Coullet, G. Iooss, M. A. Rubio and R. L. Sani for fruitful discussions. A. R. wishes to acknowledge collaboration with Drs. J. F. Colonna (LACTAMME), G. Bourhis and P. Herchuelz (CCVR) and G. P. Extremet (IMFM) in the elaboration of movie films.

REFERENCES

1. M. Pimputkar and S. Ostrach, 'Convective effects in crystals grown from melts', *J Cryst. Growth*, **55**, 614–646 (1981).
2. W. E. Langlois, 'Buoyancy-driven flows in crystal-growth melts', *Ann. Rev. Fluid Mech.*, **17**, 191–215 (1985).
3. H. Ben Hadid, B. Roux, A. Randriamampianina, E. Crespo and P. Bontoux, 'Onset of oscillatory convection in horizontal layers of low-Prandtl-number melts', in M. G. Velarde (ed.), *Physicochemical Hydrodynamics*, NATO-ASI Series, Plenum Press, New York, 1988, pp. 997–1028.
4. H. M. Ettouney and R. A. Brown, 'Finite-element methods for steady solidification problems', *J. Comput. Phys.*, **49**, 118–150 (1983).
5. M. J. Crochet, F. T. Geyling and J. J. Van Schaftingen, 'Finite-element methods for calculating the growth of semi-conductor crystals', *Fifth Int. Symp. on Finite Element Methods in Flow Problems*, Austin, TX, 1984.
6. P. M. Adornato and R. A. Brown, 'Petrov–Galerkin methods for natural convection in directional solidification of binary alloys', *Int. j. numer. methods fluids*, **7**, 761–791 (1987).
7. D. T. J. Hurle, E. Jakeman and C. P. Johnson, 'Convective temperature oscillations in molten gallium', *J. Fluid Mech*, **64**, 565–576 (1974).
8. M. A. Azouni, 'Time-dependent natural convection in crystal growth systems', *Phys. Chem. Hydrodyn.*, **2**, 295–309 (1981).

9. S. Ostrach, 'Natural convection heat transfer in cavities and cells', *Proc. Seventh Int. Heat Transfer Conf.*, Munich, Vol. 1, 1982, pp. 365–379.
10. J. J. Favier, A. Rouzaud and J. Comera, 'Influence of various hydrodynamics regimes in a melt on a solidification interface', *Rev. Phys. Appl.*, **22,** 713–718 (1987).
11. J. C. Patterson, 'On the existence of an oscillatory approach to steady natural convection in cavities', *Trans. ASME, J. Heat Transfer*, **106,** 104–108 (1984).
12. B. Staehle and E. Hahne, 'Overshooting and damped oscillations of transient natural convection flows in cavities', *Proc. Seventh Int. Heat Transfer Conf.*, Munich, Vol. 2, 1982, pp. 287–292.
13. G. Lauriat, and I. Altimir, 'A new formulation of the SADI method for the prediction of natural convection flows in cavities', *Comput. Fluids*, **13,** 141–155 (1985).
14. F. H. Busse, 'The oscillatory instability of convection rolls in a low Prandtl number fluid', *J. Fluid Mech.*, **52,** 97–112 (1972).
15. R. Clever and F. H. Busse, 'Low Prandtl number convection in a layer heated from below', *J. Fluid Mech.*, **65,** 625–645 (1974).
16. J. E. Hart, 'Stability of thin non-rotating Hadley circulations', *J. Atmos. Sci.*, **29,** 687–697 (1972).
17. J. E. Hart, 'A note on the stability of low Prandtl number Hadley circulation', *J. Fluid Mech.*, **132,** 271–281 (1983).
18. A. E. Gill, 'A theory of thermal oscillations in liquid metals', *J. Fluid Mech.*, **64,** 577–588 (1974).
19. P. Laure, and B. Roux, 'Synthèse des résultats obtenus par l'étude de stabilité des mouvements de convection dans une cavité horizontale de grande extension', *C. R. Acad. Sci., Paris, Série II*, **305,** 1137–1143 (1987).
20. K. H. Winters, 'Oscillatory convection in liquid metals in a horizontal temperature gradient', *Int. j. numer. methods eng.*, **25,** 401–414 (1988).
21. I. P. Jones, A comparison problem for numerical methods in fluid dynamics, the double-glazing problem', in R. W. Lewis and K. Morgan (eds), *Numerical Methods in Thermal Problems*, Pineridge Press, Swansea, 1979, pp. 338–348.
22. I. P. Jones, 'Low Prandtl number free convection in a vertical slot', *AERE Harwell Report R-10416*, 1982.
23. P. M. Gresho and C. D. Upson, 'Application of a modified finite element method to the time-dependent thermal convection of a liquid metal', *Third int. Conf. on Numerical Methods in Laminar and Turbulent Flows*, Seattle, WA; also in *UCRL-88990*, 1983.
24. M. J. Crochet, F. T. Geyling and J. J. Van Schaftingen, 'Numerical simulation of the horizontal Bridgman growth. Part I: Two-dimensional flow', *Int. j. numer. methods fluids*, **7,** 29–48 (1987).
25. S. Dupont, J. M. Marchal, M. J. Crochet and F. T. Geyling, 'Numerical simulation of the horizontal Bridgman growth. Part II: Three-dimensional flow', *Int. j. numer. methods fluids*, **7,** 49–67 (1987).
26. H. Ben Hadid and B. Roux, 'Oscillatory buoyancy-driven flow in horizontal liquid-metal layers', *ESA-SP-256*, 1987, pp. 477–485.
27. E. Crespo del Arco, 'Contribución al estudio de inestabilidades termohidrodinamicás en fluidos newtonianos y viscoelásticos en capas horizontales y cilindros, *Tesis Doctoral*, UNED, Madrid, 1987.
28. K. H. Winters, 'Oscillatory convection in crystal melts: the horizontal Bridgman process', *Fifth Int. Conf. on Numerical Methods in Thermal Problems*, Montreal, 1987; also in Harwell Report T.P. 1230.
29. J. M. Vanel, R. Peyret and P. Bontoux, 'A pseudo-spectral solution of vorticity–streamfunction equations using the influence matrix technique', in K. W. Morton and M. J. Baines (eds.), *Numerical Methods for Fluid Dynamics II*, Clarendon Press, Oxford, 1986, pp. 463–475.
30. A. Randriamampianina, P. Bontoux and B. Roux, 'Ecoulements induits par la force gravifique dans une cavité cylindrique en rotation', *Int. J. Heat Mass Transfer*, **30,** 1275–1292 (1987).
31. G. De Vahl Davis, 'Finite-difference methods for natural and mixed convection in enclosures', *Heat Transfer 86*, Hemisphere, Washington DC, 1986, pp. 101–109.
32. S. Ostrach, 'Convection phenomena at reduced gravity of importance for materials processing', *Proc. Second Eur. Symp. on Material Sciences in Space, ESA-SP-114*, 1976.
33. D. Gottlieb and S. A. Orszag, *Numerical Analysis of Spectral Methods: Theory and Application*, CBMS Regional Conference Series in Applied Mathematics, SIAM, 1977.
34. R. Peyret and T. D. Taylor, *Computational Methods for Fluid Flows*, Springer-Verlag, New York, 1983.
35. C. Canuto, A. Quarteroni, M. Y. Hussaini and T. A. Zang, *Spectral Methods in Fluid Dynamics*, Springer-Verlag, New York, 1988.
36. J. P. Pulicani, 'Application des méthodes spectrales à l'étude d'écoulements de convection', *Mémoire de Thèse*, Université de Nice, 1988.
37. C. Temperton, 'Fast mixed-radix real Fourier transforms', *J. Comput. Phys.*, **52,** 340–350 (1983).
38. C. W. Gear, *Numerical Initial Value Problems in Ordinary Differential Equations*, Prentice-Hall Series in Automatic Computation (edited by G. E. Forsythe), Englewood Cliffs, NJ, 1971.
39. A. C. Hindmarsh, 'LSODE and LSODI: two new initial value ordinary differential equation solvers', *ACM-SIGNUM Newsletter*, **15,** 10–11 (1980).
40. L. R. Petzold, 'Automatic selection of methods for solving stiff and non stiff systems of ordinary differential equations', *Sandia, Nat. Lab. Report SAND80-8230*, 1980.
41. G. D. Byrne and A. C. Hindmarsh, 'Stiff ODE solvers: a review of current and coming attractions', *J. Comput. Phys.*, **70,** 1–62 (1987).
42. J. Ouazzani, R. Peyret and A. Zakaria, 'Stability of collocation–Chebyshev schemes with application to the Navier–Stokes equations', *Notes on Numerical Fluid Mechanics Vol. 13*, Vieweg, Braunschweig, 1985, pp. 287–294.

43. U. Ehrenstein, 'Méthodes spectrales de résolution des équations de Stokes et de Navier–Stokes: application à des écoulements de convection double-diffusive', *Mémoire de Thèse*, Université de Nice, 1986.
44. U. Ehrenstein, and R. Peyret, 'A Chebyshev–collocation method for the Navier–Stokes equations with application to double-diffusive convection', *Int. j. numer. methods fluids*, **9**, 427–452 (1989).
45. D. B. Haidvogel and T. Zang, 'The accurate solution of Poisson's equation by expansion in Chebyshev polynomials', *J. Comput. Phys.*, **30**, 137–180 (1979).
46. P. M. Gresho and R. L. Sani, private communication, 1984.
47. B. Roux, P. Bontoux and D. Henry, 'Numerical and theoretical study of different regimes occurring in horizontal fluid layers differentiallv heated', *Lecture Notes in Physics, Vol. 230*, Springer-Verlag, New York, 1984, pp. 202–210.
48. M. D. Neary and K. D. Stephanoff, 'Shear-layer-driven transition in a rectangular cavity', *Phys. Fluids*, **30**, 2936–2946 (1987).
49. A. Randriamampianina, E. Crespo del Arco, J. P. Fontaine and P. Bontoux, P. 'Spectral method for two-dimensional time-dependent $Pr \rightarrow 0$ convection', in B. Roux (ed.), *Notes on Numerical Fluid Mechanics Vol 27*, Vieweg, Braunschweig, 1989, pp. 245–255.
50. E. Crespo del Arco, A. Randriamampianina and P. Bontoux, 'Two-dimensional simulation of time-dependent convective flow of a $Pr \rightarrow 0$ fluid. A period doubling transition to chaos', in M. G. Velarde (ed.), *Synergetics, Order and Chaos*, World Scientific, London, 1988, pp. 244–257. See also in ESA SP-295, ESA Noordwijk, 1990, p. 219.
51. V. Arnold, *Chapitres Supplémentaires de la Théorie des Equations Différentielles Ordinaires*, MIR, Moscow, 1980.
52. R. L. Sani, and B. Carpenter, private communication, 1988.
53. E. Crespo del Arco, R. Peyret, J. P. Pulicani and A. Randriamampianina, 'Spectral calculations of oscillatory convective flows', in T. J. Chung and G. R. Karr (eds), *Finite Element Analysis in Fluids (Proc. 7th Int. Conf. on Finite Element Methods in Flow Problems)*, UAH Press, Huntsville, AL, 1989, pp. 1464–1472.
54. J. P. Pulicani and R. Peyret, 'Spectral calculations of convection in low-Pr fluids', in B. Roux (ed.), *Notes on Numerical Fluid Mechanics Vol. 27*, Vieweg, Braunschweig, 1989, pp. 237–244.
55. B. Roux, H. Ben Hadid and P. Laure, 'Hydrodynamical regimes in metallic melts subject to a horizontal temperature gradient', *Eur. J. Mech.*, **8**, 375–396 (1989).